

20 Abstract

21 Suspended sediments (SS) contribute to the maintenance of several ecosystems. However,
22 intense soil erosion can lead to environmental, social, and economic impacts. South America
23 (SA) has very high erosion and sediment transport rates. Here we present a detailed description
24 of the spatio-temporal dynamics of natural SS flows in SA using the continental sediment model
25 MGB-SED AS. We evaluate the model with daily in-situ data from 595 stations, information
26 from regional studies and a global model. The model performance analysis showed that, in
27 general, there was a better agreement between simulated and observed data than with the
28 information found in regional studies and of the global model. The use of the hydrodynamic
29 propagation method has allowed a better representation of sediment flows in rivers and
30 floodplains. Based in the calibrated model results, SA delivers 1.00×10^9 t/year of SS to the
31 oceans, in which the Amazon (4.36×10^8 t/year), Orinoco (1.37×10^8 t/year), La Plata (1.11×10^8
32 t/year) and Magdalena (3.26×10^7) rivers are the main suppliers. The floodplains play an essential
33 role, retaining about 12% (2.40×10^8 t/year) of the SS loads reaching the rivers. In this study,
34 datasets related to SS flows in SA were generated and can be used to support other large-scale
35 researches or policymakers and stakeholders for adequate management of continental land use.
36 **Key words:** Continental-scale; Erosion; MUSLE; MGB

37

38 1 Introduction

39 Understanding erosion and sediment transport processes are relevant to comprehend geological
40 changes and landscape evolution (Latrubesse et al., 2005; Syvitski and Milliman, 2007; Zhang et
41 al., 2004), biogeochemical cycles (e.g., Beusen et al., 2005; Doetterl et al., 2012; Galy et al.,
42 2015; Ito, 2007; Kuhn et al., 2009; Lal, 2003; Müller-Nedebock and Chaplot, 2015; Naipal et al.,
43 2018; Tan et al., 2017; Van Oost et al., 2007; Willenbring and Von Blanckenburg, 2010), and
44 impacts of human activities, such as land use/ land cover changes (e.g., Murphy, 2019; Oliveira
45 et al., 2015; Panagos et al., 2017; Wang and Van Oost, 2019) and dams construction (e.g., Best,
46 2019; Cohen et al., 2014; Forsberg et al., 2017; García-Ruiz et al., 2015; Latrubesse et al., 2017,
47 2005; Restrepo et al., 2006; Syvitski et al., 2005). In the last 8,000 years, the conversion of
48 natural vegetation into agriculture has resulted in an accumulated erosion of about $27,187 \pm 9,030$
49 Gt worldwide (Wang and Van Oost, 2019). Meanwhile, it is estimated that the impact of soil
50 erosion on global GDP (Gross Domestic Product) is an annual loss of ~US\$ 8 billion,
51 threatening the food security, leading to a global reduction in the production of 33.7 Gt/year and
52 a consequent increase in water withdrawals of 48 billion m³/year (Sartori et al., 2019).

53 A large number of rivers with the largest sediment transports in the world (>100 Mt/year) are in
54 South America (SA, Borrelli et al., 2017; Doetterl et al., 2012; Latrubesse et al., 2005; Mouyen
55 et al., 2018; Naipal et al., 2018; Syvitski et al., 2014, 2005; Wuepper et al., 2019). The Amazon
56 River is at the top of the list (Latrubesse et al., 2005), transporting about 555 Mt/year at Óbidos
57 (Filizola and Guyot, 2009).. Borrelli et al. (2017) observed high erosion rates (>10 t/ha.year) in
58 SA in 2012, which increasing tendency compared to the 2001 year. This severe erosion has
59 contributed to generate, for example, a reduction in food production of 8,170 Mt/year in Brazil
60 (Sartori et al., 2019). Researches have shown that climate changes will impact the land use/ land
61 cover (Almagro et al., 2017; Brêda et al., 2020; Cohen et al., 2014) and that the implementation
62 of many dams will affect the connectivity of water flows even more, sediments, nutrients, and
63 aquatic organisms (Forsberg et al., 2017; Grill et al., 2019; Latrubesse et al., 2017).

64 In the last decades, great efforts have been dedicated to understanding and quantifying sediment
65 loads around the world. The use of in-situ measured data is one of the main tools used to
66 estimate the transport in rivers (e.g., Best, 2019; Dearing and Jones, 2003; Latrubesse et al.,
67 2005; Mouyen et al., 2018; Murphy, 2019; Niu et al., 2014; Restrepo et al., 2006) or watershed
68 erosion rates (e.g., García-Ruiz et al., 2015). However, there is a lack of measurements of
69 sediments in both intra-basin (e.g., García-Ruiz et al., 2015; Kettner et al., 2010; Lima et al.,
70 2005) and near the Oceans, where less than 10% of rivers have monitoring of sediment delivery
71 to coastal zones (Syvitski et al. 2005). Notably, in the era of big data and big science, there are
72 still a lack of hydrological, sediment, and nutrient data available in the world's large rivers (Best,
73 2019). The lack of data represents a major barrier to develop analyses for large scales
74 (continental or global) that require long time series (Dearing and Jones, 2003).

75 Computational sediment models have helped to fill this gap of sediment information. For the
76 global scale, several applications have been carried out with Universal Soil Loss Equation
77 (USLE, e.g., Xiong et al., 2019, 2018) – developed by Wischmeier and Smith (1978) – and its
78 revised version RUSLE (e.g., Borrelli et al., 2017; Naipal et al., 2018, 2015; Sartori et al., 2019;
79 Wuepper et al., 2019; Yang et al., 2003). According to Alewell et al. (2019), USLE and RUSLE
80 are the most used models around the world. However, approaches that used these models were
81 focused only on soil loss spatial representation, with long-term average estimates, which do not
82 allow to understand the dynamic processes that involve sediment flows, such as the loads
83 transported by the rivers. In this perspective, global sediment transport models were developed to
84 estimate the impact of human activities on sediment delivery to the oceans (Syvitski et al. 2005),
85 characterize rivers in terms of transported sediment loads (Cohen et al., 2013; Pelletier, 2012),
86 and assess regional trends and variabilities (Cohen et al. 2014). The global models are generally
87 empirically-based and have few input parameters, which facilitate applications on these scales.
88 Nevertheless, these models have been poorly validated, they were focused on estimating long-
89 term annual averages (e.g., Cohen et al. 2013; Pelletier 2012; Syvitski and Milliman 2007), and
90 are based on simplified methodologies to estimate hydrological variables and sediment routing.

91 Despite the barriers encountered in the model applications on a global scale, few papers are
92 found in the literature regarding continental scales. Panagos et al. (2015) used the RUSLE2015
93 model to estimate erosion rates for the reference year 2010 across Europe, with a spatial
94 resolution of 100 m. Campagnoli (2006) used an approach (not fully described) focused on
95 geological and geomorphological aspects to generate an annual sediment yield map of South
96 America. However, as mentioned in the previous paragraph, these approaches are not capable to
97 fully describe dynamic sediment processes.

98 The global model WBMsed used by Cohen et al. (2014) uses the simplified Muskingum-Cunge
99 routing method (Wisser et al., 2010). The global models of Pelletier (2012) and Syvitski and
100 Milliman (2007) do not explicitly consider the rivers flow routing. Studies performed in several
101 South America regions have shown that simplified methods are sometimes not suitable to
102 represent backwater and floodplain effects, which can be driving factors in flow routing in large
103 basins (e.g., Angarita et al., 2018; Bravo et al., 2012; Paiva et al., 2013, 2011; Pontes et al., 2017;
104 Siqueira et al., 2018; Zhao et al., 2017).

105 On the other hand, when we compare the sediment modeling studies with hydrological-
106 hydrodynamic modeling studies, one can see that significant advances have been made in the
107 later for global and continental scales. For example, studies made by Hanasaki et al. (2006),
108 Hanasaki et al., (2008a, 2008b) and Hanasaki et al. (2018) showed global scale simulations with

109 many capabilities to represent the global hydrological cycle and the human interference on it,
110 such as water abstractions and rivers impoundments. The van Beek et al. (2011) study used the
111 global PCR-GLOBWB model to evaluate water availability and water stress on a monthly scale
112 for the whole globe. Meanwhile, the study by Beck et al. (2017) shows how extensive global
113 hydrological models development research is, while evaluating the runoff estimates generated
114 across the globe by six global models in addition to four land surface models. Other examples,
115 with a greater focus on the fluvial hydrodynamic representation, are the studies of Yamazaki et
116 al. (2011) and Yamazaki et al. (2013), which showed global model applications for flooding
117 applications, including the impact of floodplains. Also, most of the models developed in recent
118 years simulate processes on a daily scale (Bierkens, 2015). Many of them have the concept of
119 "hyperresolution models" as their motivation, which aims to simulate processes on a global
120 scale, but whose results are useful on a local scale (e.g., Bates et al., 2018; Wada et al., 2014;
121 Wood et al., 2011).

122 On the continental scale, progress in the development of hydrological and hydrodynamic models
123 also stand out, with dam representation (Shin et al., 2019) and improvements in fluvial
124 hydrodynamics (Siqueira et al., 2018). The National Water Model (NWM,
125 <http://water.noaa.gov/about/nwm>) developed in 2016 by National Oceanic and Atmospheric
126 Administration (NOAA), which has been conducting simulations and streamflow forecasts for
127 the United States, can be mentioned as an example. The study of Siqueira et al. (2018) applied
128 for the first time a continental-scale fully coupled hydrological-hydrodynamic model for the
129 whole South America. The Siqueira et al. (2018) results showed that limitations on flow
130 estimation by state-of-the-art global models could be reduced using better calibrated continental
131 models, which represent relevant processes (e.g., hydrodynamics) for the area of interest, and
132 which are built on previous experience of regional-scale studies.

133 While these cited examples of hydrologic and hydrodynamic modeling with continental and
134 global scales have increasingly appeared in the literature, including the goal of attaining
135 "hyperresolution" models, no study has been found in the literature to estimate continental-scale
136 sediment transport having hydrologic-hydrodynamic processes integrated. There is then a gap
137 between the advances in large scale hydrologic and hydrodynamic modeling and the advances in
138 sediment modeling at continental and global scales.

139 Bridging the gaps between recent advances in hydrologic and hydrodynamic modeling at
140 continental scales and sediment modeling provide some opportunities: (i) obtain models that
141 allow the comprehension and comparison of spatial and temporal dynamics explicitly, and that
142 still represent important processes such as backwater effects in the rivers and the lateral flow
143 exchange of water and sediments with floodplains (e.g., Buarque, 2015; Cohen et al., 2013; Grill
144 et al., 2019; Paiva et al., 2013, 2011; Pontes et al., 2017; Rudorff et al., 2018); (ii) obtain
145 continental or global scale models that are well-validated to provide locally relevant information
146 at multiple time scales and suitable for policymakers and stakeholders (Bierkens, 2015;
147 Fleischmann et al., 2019b; Siqueira et al., 2018); (iii) acquire continental sediment discharges
148 information not only in the outlets of large rivers but also intra-basin. These items, therefore,
149 become the interest of this study, which has South America as a subject of study, and aims to
150 answer the following specific questions from modeling results: what is the accuracy of the
151 proposed continental sediment model? What are the potential transported loads by the rivers in
152 the continent? What are the spatial and temporal dynamics of sediment flows over South
153 America? What is the impact of fluvial hydrodynamics on sediment transport and deposition? In

154 which regions do suspended sediments deposit the most? To answer these questions, we have
155 developed and evaluated the performance of sediment erosion and transport model for the entire
156 South American domain.

157 **2 Overview of Sediment-Related Processes in South America**

158 South America (SA) transports ~20% of the sediments reaching the oceans (Syvitski et al.,
159 2005), and the Amazon and Magdalena rivers (Figure 1-a) are among the world's largest
160 sediment delivers (Mouyen et al., 2018). SA has the second-highest potential erosion rate on the
161 planet and the highest increase in the last century (Wuepper et al., 2019). This increase also
162 attributes to SA the highest rate of particulate organic carbon erosion. (Naipal et al., 2018).
163 Among the causes of these changes are agricultural expansion and deforestation (Borrelli et al.,
164 2017), which have been increasing, causing concerns in the Amazon basin (Aguiar et al., 2016;
165 Aragão, 2012).

166 Most of the SA is located in tropical regions that have little interannual variability between
167 sunrise and sunset and receive high solar incidence. The Intertropical Convergence Zone (ITCZ)
168 directly influences the establishment of dry and rainy seasons; El Niño events; and the South
169 Atlantic Convergence Zone (SACZ), which causes heavy precipitations in the summer. Annual
170 precipitation variability is strong, with desert regions in Chile and rainfall reaching
171 approximately 10,000 mm in Colombia (Latrubesse et al., 2005).

172 Rivers that drain the Andean region transport the highest sediment load on the continent.
173 According to Restrepo et al. (2006), the Magdalena River is the one with the highest average
174 sediment yield (690 t/km².year). More than 90% of the suspended sediment (SS) load of the
175 Amazon Basin comes from the Andes (Latrubesse et al., 2005). Filizola and Guyot (2011), using
176 in-situ measured data, indicate that the Madeira River (Figure 1-a) contributes almost 50% to the
177 Amazon River solid discharge, in which the Beni and Mamoré rivers represent about 72% and
178 28%, respectively, of the Madeira transport. (Guyot et al., 1999). The Ucayali River drains the
179 Peruvian Andean part and is also one of the SA rivers with the highest SS load (Latrubesse et al.,
180 2005). Rivers originating in the South Andean regions also carry high SS loads, such as the
181 Bermejo River, which provides about 90% (Amsler and Drago, 2009) and the Pilcomayo river
182 about 140 Mt/year of the total load carried by the Paraná River (Latrubesse et al., 2005). Lima et
183 al. (2005) observed that smaller rivers like Parnaíba, Paraíba do Sul and Doce (Figure 1-a),
184 although they do not have the highest sediment yield rates (t/year.km²), they have high values of
185 suspended sediment concentrations (SSC) (Lima et al. 2005). According to Latrubesse et al.
186 (2017), Cratonic rivers such as the Negro, Tapajós and Xingu present low SS loads. At the same
187 time, the Araguaia (Latrubesse et al., 2005), Tocantins (Latrubesse et al., 2005), Paraná (Amsler
188 and Prendes, 2000) and Orinoco (Meade et al., 1990) rivers have intermediate values of SS yield.

211 Despite the knowledge provided by previous studies, some things are not yet fully understood:
212 the effect of fluvial hydrodynamics on sediment flows; thoroughly and accurately, the
213 spatiotemporal patterns of denudation rates, concentration (SSC), solid discharge (QSS) and
214 suspended sediment deposition; the driving factors in the relation between SSC/QSS and water
215 discharge; the annual sediment balance of the SA and its main rivers; the potential consequences
216 of climate changes on the patterns of these variables; the impact of dams on rivers and those with
217 the greatest potential to be affected; the relevance of landslides in the sediments transport of each
218 river; and the relative contribution of the anthropic activities, such as mining, to the sediment
219 flows.

220 **3 South America Sediment Model**

221 To elucidate the South America sediment flows, we used the MGB-SED sediment model
222 (Buarque, 2015; Fagundes et al., 2019, 2020; Föeger, 2019) coupled to hydrologic-
223 hydrodynamic model MGB AS, presented by Siqueira et al. (2018). This modeling configuration
224 was chosen for three main reasons: (i) it is the first fully coupled hydrologic-hydrodynamic
225 model, developed for regional scales, applied for South America's continental domain; (ii) the
226 model has a high temporal resolution (daily outputs) and was validated in most of SA using in-
227 situ and other sources of hydrological data, showing that hydrological variables were well
228 represented; and (iii) the performance of sediment models can be strongly affected by the
229 performance of hydrological models (Cohen et al., 2013; Shen et al., 2012), and the MGB AS
230 has a better performance compared to the global models evaluated by Siqueira et al. (2018).

231 3.1 MGB AS Hydrologic-Hydrodynamic Model

232 The *Modelo Hidrológico de Grandes Bacias* (MGB) was initially developed by Collischonn et
233 al. (2007) and further improved to address different questions (e.g., Fleischmann et al., 2019,
234 2018; Paiva et al., 2011; Pontes et al., 2017; Siqueira et al., 2018). It is a conceptual model, semi-
235 distributed, and has spatial discretization defined by unit catchments (Pontes et al., 2017), each
236 with its own river stretch and floodplain. Precipitation is the main driver of the model (it does not
237 consider snow or ice melting), from which hydrological processes are simulated, such as: canopy
238 interception, soil infiltration, evapotranspiration, and routing of surface, subsurface and
239 groundwater flows. Each unit catchment can have several Hydrological Response Unit (HRU),
240 which is a combination of soil type and soil cover (Kouwen et al., 1993), where water and energy
241 are computed. Surface, subsurface, and groundwater volumes are stored in simple linear
242 reservoirs and further routed to the stream network.

243 In the following, a brief description of the methodology used by Siqueira et al. (2018) is
244 presented. We use the same MGB AS settings and structure, as well as the input data used by the
245 authors. They found agreement between the simulated and observed flows that resulted in a
246 Nash-Sutcliffe efficiency coefficient (NSE) > 0.6 in more than 55% of the analysed stations.

247 Flow routing in the drainage network is performed using the local inertial method (Bates et al.,
248 2010; Pontes et al., 2017). The continuity equation is used to estimate the stored volume, flooded
249 area, and streamflow and floodplain water level. Floodplains are represented as storage areas that
250 compute evaporation in open waters, assuming that water level is constant for the whole unit
251 catchment. Floodplains water infiltration for unsaturated soils are still considered (as described
252 by Fleischmann et al., 2018), specifically for the Pantanal wetlands.

253 MGB AS model also allows using the Muskingum-Cunge (MC) method to routing flows. This
 254 method takes a time interval that is subdivided into smaller intervals and also split the total river
 255 reach length into sub-reaches to route the flows. The MC method enables the representation of
 256 flood wave translation and smoothing, that routes at a velocity c (celerity) higher than average
 257 streamflow velocity in a specific time interval and river reach. Among the method advantages
 258 are the more straightforward implementation, lower computational efforts, and numeric stability.
 259 As for disadvantages, there are the non-representation of backwater effects and lateral exchanges
 260 between river and floodplain, which may play an important role in large basins (Getirana and
 261 Paiva, 2013).

262 MGB-SA was built using the 15 arcsec HydroSHEDS flow direction map (Lehner et al., 2008)
 263 and a minimum drainage area threshold of 1,000km², and basins were discretized into unit-
 264 catchments with fixed river lengths equal to 15 km (Siqueira et al., 2018). The Digital Elevation
 265 Model (DEM) Bare-Earth SRTM v.1 (O’Loughlin et al., 2016) was used to compute the Height
 266 Above Nearest Drainage (HAND), from which the floodplain topography was estimated at a sub-
 267 grid level. River hydraulic geometry was set using the global data set of Andreadis et al. (2013),
 268 enhanced using information from regional studies (Beighley and Gummadi, 2011; Paiva et al.,
 269 2013, 2011; Pontes, 2016).

270 Precipitation data from global Multi-Source Weighted Ensemble Precipitation – MSWEP v1.1
 271 (Beck et al., 2017) were used. The climatic variables used to estimate evapotranspiration were
 272 temperature, atmospheric pressure, income shortwave solar radiation, relative humidity, and
 273 wind speed obtained from Climate Research Unit (CRU) Global Climate v.2 (New et al., 2002).
 274 They are long-term monthly averages (1961-1990) and have 10’ spatial resolution. South
 275 America HRUs map from Fan et al. (2015) was used to represent soil type (shallow and deep)
 276 and soil cover.

277 For more details about approaches, equations, and data, a full description can be found in
 278 Siqueira et al. (2018).

279 3.2 MGB-SED sediment model

280 The *Modelo de Sedimentos de Grandes Bacias* (MGB-SED) was introduced by Buarque (2015)
 281 and improved in other studies (e.g., Fagundes et al., 2020; Fagundes et al., 2019; Föeger, 2019).
 282 The MGB-SED has three modules (basin, river and floodplain) and enables the simulation of rill
 283 and interrill erosion processes in hillsides, bed river erosion and deposition, sediment transport
 284 through the river network, and deposition of suspended sediment in the floodplains.

285 The sediment volumes from hillsides to river reaches in each unit catchment is the primary
 286 information estimated by the model using the Modified Universal Soil Loss Equation (MUSLE)
 287 (MUSLE, Williams, 1975) :

$$288 \quad Sed = \alpha \cdot (Q_{sur} * q_{peak} * A)^{\beta} \cdot K \cdot C \cdot P \cdot LS_{2D} \quad (1)$$

289 where Sed [t/day] is the sediment yield, Q_{sur} [mm/day] is the specific runoff volume, q_{peak} [m³/s]
 290 is the peak runoff rate, A [ha] is the unit catchment area, K [0.013.t.m².h./m³.t.cm] is the soil
 291 erodibility factor, C [-] is the cover and management practices factor, P [-] is the conservation
 292 practices factor, LS_{2D} [-] is a bidimensional topographic factor; and α and β are the fit
 293 coefficients of the equation (which are calibrated afterward), whose values originally estimated
 294 by Williams (1975) were 11.8 and 0.56, respectively.

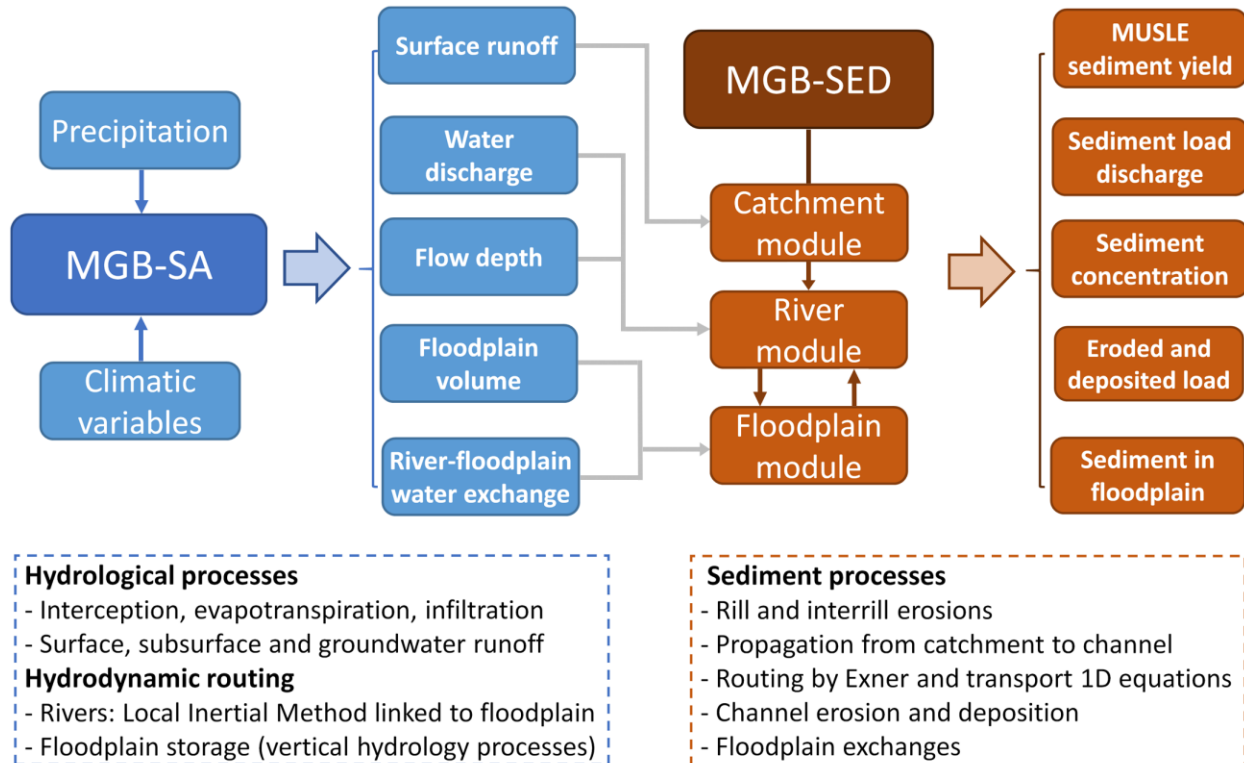
295 Q_{sur} and q_{peak} values are estimated by the coupled hydrologic model (MGB AS in this study). P
296 factor is estimated from the knowledge of soil management and conservation practices but has
297 been adopted as 1 in most large scale applications (e.g., Benavidez et al. 2018; Borrelli et al.
298 2017; Naipal et al. 2015; Phinzi and Ngetar 2019). C factor is usually calculated from field
299 experiments but has been usually adopted from literature for each soil cover, as presented by
300 Benavidez et al. (2018) and Phinzi and Ngetar (2019). MGB-SED model computes K factor
301 from Williams (1995) equation, in which considers the soil texture (sand, silt and clay
302 percentages) and amount of soil organic carbon. LS_{2D} factor is estimated by the model using a
303 DEM (Buarque, 2015) and more details about the LS_{2D} estimates can be verified in the
304 supplementary material S1.

305 The approach used by MGB-SED to estimate sediment yield using MUSLE equation is the same
306 used in other models, as SWAT (Arnold et al., 1998), CREAMS (Knisel, 1980), PERFECT
307 (Littleboy et al., 1992) and SWIM (Krysanova et al., 1998). We are aware of the known
308 limitations of this approach, as it does not explicitly consider all erosive processes such as those
309 related to mass movements. Some authors like Tan et al. (2018) have already improved the
310 estimates of a sediment model by including the representation of shallow landslides. However, as
311 an initial approach and because it has already presented itself sufficiently in other large-scale
312 modeling applications (e.g., Buarque, 2015), we use it, and we are aware of the limitations it
313 imposes on the analysis of the results.

314 After computing sediment yield by MUSLE, the estimated volume is divided into three classes
315 of particle sizes (silt, clay and sand), according to the percentage of these classes in the soil.
316 Three linear reservoirs (one for each class) are used for the sediment routing from the hillsides to
317 the drainage network. Each soil particle size is then routed from upstream to downstream using
318 the following approaches: (i) for the fine loads (silt and clay), the unidimensional transport
319 equation without the diffusion term is used, and the sediments are transported in suspension,
320 without deposition in the channel; (ii) for sand, considered as bed load, the Exner sediment
321 continuity equation is used together with the Yang transport capacity equation (Yang, 1973) to
322 quantify the transport in the channel, the erosion or deposition in the bed. It is worth mentioning
323 that in this study only the transport of suspended sediment load (silt+clay) is evaluated.

324 In the floodplains, a zero longitudinal velocity is assumed, and only river-floodplain exchanges
325 are possible. The perfect mixing in the floodplains is also assumed, which implies constant
326 concentrations of silt and clay in the vertical profile. Floodplains work as storage areas, where
327 fine particles can be deposited but cannot be resuspended. Sediment deposition in the floodplains
328 is estimated considering the fall velocity proposed by Wu and Wang (2006). Sediments that do
329 not deposit flow back to the main channel.

330 More details about model equations can be found in the supplementary material S1. A summary
331 of the coupling between the two models that resulted in the MGB-SED AS, main input data,
332 processes, and outputs are shown in Figure 2.



333

334 **Figure 2:** MGB-SED AS scheme. The blue (brown) part is related to the hydrological (sediment) model, its
 335 structure, main input data, processes, and main outputs.

336

3.3 Simulation Input Datasets

337 MGB-SED model requires topographic, soil type, texture and cover, and surface runoff to
 338 estimate daily sediments using the MUSLE equation. To compute K factor (Figure 3-a), we use
 339 percentages of silt, clay, sand and organic carbon for each soil type from the Food and
 340 Agriculture Organization (FAO) of the United Nations (FAO/UNESCO, 1974). LS_{2D} factor
 341 (Figure 3-b) was estimated using Bare-Earth SRTM v.1 DEM (O’Loughlin et al., 2016). We use
 342 each land cover identified in URH South America map (Fan et al., 2015) to compute C factor
 343 (Figure 3-c) based on previous studies (Benavidez et al., 2018; Buarque, 2015; Fagundes et al.,
 344 2019). It is worth mentioning that C values for the forest were not the same throughout SA, due
 345 to the heterogeneity of forest coverings (see Figure S1 - Supporting Information). P factor was
 346 adopted equal to 1, since in that scale there is no detailed information about soil conservation
 347 practices.

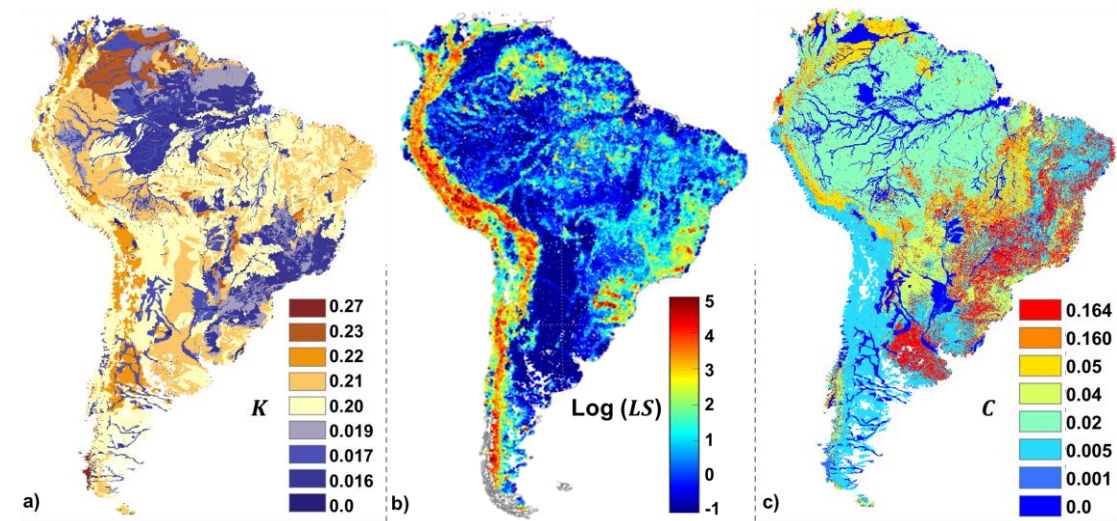


Figure 3: MUSLE parameters adopted for South America: a) K [0.013.t.m².h./m³.t.cm] factor; b) $\text{Log}(LS_{2D})$ [-] factor; and c) C [-] factor.

As mentioned before, the daily runoff was estimated by MGB AS and it was also used to compute q_{peak} . From this data and other simulated hydrological variables (e.g., river discharge and water level, and floodplains stored volumes), it was possible to compute soil loss and sediment transport using the same spatial discretization of MGB AS. We have chosen to change the values of the adjustable parameters α and β , as it has been done in several works (see the review presented by Sadeghi et al. (2014)), including previous applications with the MGB-SED model (e.g., Fagundes et al., 2019).

3.4 Experimental Design

3.4.1 Model Calibration and Evaluation

The base period for the analysis and performed simulations using the MGB-SED AS model was 1990-2009, in which the first two years were used to warm up the model. Initially, we performed a mass balance to check if the model was generating numerical errors, adding or removing mass in the simulation.

In order to know the natural (without impoundments) simulated sediment loads transported by the rivers, it was necessary to evaluate the performance of the MGB-SED AS model. For that, we used suspended sediment discharge (QSS) of the 595 in-situ stations (Figure 1-b) in Brazil - ANA (450), Colombia - IDEAM (109) and Argentina - BDHI (36). Suspended sediment is measured using cross-sectional mean sediment mass concentration, using the ISO 4363 (2002) protocol as reference. There are differences depending on river width and discharge. The main difference is found for IDEAM information, in which daily surface samples are taken and correlated against cross-sectional mean sediment mass concentration (IDEAM, 2007). ANA, BDHI, and IDEAM provide information of suspended sediment quarterly, monthly, and daily, respectively. Moreover, as samples are often not collected during flood events (in cases of ANA and BDHI), time series may be biased due to the predominance of data from the dry period. To address this continental sediment modeling we assume that uncertainties related to different sampling methods are not enough to prevent a comparison against modeling results.

377 To increase confidence and consistency, we used only databases for which samples are taken
 378 from the whole cross-section, or data are derived from the latter. Both observed data and
 379 simulations do not consider the organic solids. Free sediment data from other countries were not
 380 found. To better explore the data, stations having at least 4 measurements in the period of 1992-
 381 2009 and drainage area above 1,000 km² were selected.

382 In the calibration (2002-2009), 77 stations were used, with drainage areas ranging from 3,045 to
 383 4,700,503 km². The calibration stations were selected as follows: i) we always choose stations
 384 with the largest drainage area for each monitored sub-basin; ii) in case stations were located
 385 downstream of one (or more) reservoir (Figure 1), the one upstream with the largest drainage
 386 area would be used; iii) when there was just one station in a sub-basin, it was used to calibrate
 387 the model.

388 The calibration was performed in two stages: an automatic calibration followed by a manual
 389 calibration. Automatic calibration was performed using the MOCOM-UA optimization algorithm
 390 (Yapo et al., 1998) following the recommendations proposed by Fagundes et al., (2019). The
 391 algorithm MOCOM-UA requires setting some parameters and initial conditions. We used a
 392 population of 100 individuals; three objective functions - Nash-Sutcliffe efficiency (*NSE*, Nash-
 393 Sutcliffe, 1970) efficiency coefficient, *BIAS*, and error in the slope of the duration curve between
 394 10% and 50% (*DCPerm*, Kollat et al., 2012); maximum of 500 iterations; and three calibration
 395 parameters: α and β (Equation 1) and Υ (Equation 2). These parameters were adjusted to each
 396 model sub-basin.

$$397 \quad \mathfrak{t} = \Upsilon \cdot TKS \quad (2)$$

398 *TKS* (s) is the parameter which indicates the delay time of the surface linear reservoir output
 399 (Collischonn et al., 2007); \mathfrak{t} (s) indicates the travel time of the sediments to the drainage network
 400 (see Text S1 in the support information S1); Υ [-] is the adjustment factor between the two
 401 aforementioned parameters. It means that surface runoff and sediment load transport can have
 402 different travel times between the hillsides and channels, and Υ can increase or decrease this
 403 difference. This approach is used to better represent the sediment processes, and overcome some
 404 limitations due to the use a large-scale sediment model. The range of values used for the
 405 calibration parameters α , β and Υ was, respectively, 0.01-25.0, 0.1-0.5 and 0.1-5.0.

406 For the basins where we have not data, a simple transfer of parameters from the calibrated sub-
 407 basins was made. The transfer process was based on the physical and climatic characteristics of
 408 the region.

409 For the validation (1992-2009), the same criteria of the calibration stage were used, resulting in
 410 the selection of 56 sediment stations. A global evaluation of the model performance was also
 411 carried out using the 595 stations. It was a conservative decision, which includes the model
 412 evaluation for the 1992-2009 period with the stations used (77) and those not used (518) in the
 413 calibration process. In addition to the metrics already mentioned, the model performance was
 414 evaluated using Pearson's correlation coefficient (*r*), Kling-Gupta (*KGE*) efficiency coefficient
 415 and relative value of Root Mean Square Error (*RMSE*).

416 MGB-SED AS results were compared to estimates from several regional studies (see Table S1 -
 417 Supporting Information). The comparison was performed using data of long-term average annual
 418 QSS from 80 sites exceeding a drainage area of 5,000 km² (see Table S1 and Figure S2,

419 Supporting Information). The agreement between QSS simulated and those of regional studies
 420 was evaluated from the relative difference between the annual values (Equation 3).

$$421 \quad Diff(\%) = 100x \frac{QSS \text{ MGB-SED AS} - QSS \text{ reg. studies}}{QSS \text{ reg. studies}} \quad (3)$$

422 Positive (negative) *Diff* values mean that MGB-SED AS model calculated values higher
 423 (lower) than those from regional studies used in the comparison.

424 QSS simulated was also compared to the outputs of the global sediment model WBMsed (Cohen
 425 et al., 2014). This model was selected because it is the only one with data freely available for
 426 society. It is a grid model with 6 arc-min (~11km) spatial resolution and uses the Muskingum-
 427 Cunge method to route daily water streamflows (Wisser et al., 2010). To estimate the QSS,
 428 firstly, the model computes the long-term average values using global empirical equation
 429 BQART (Syvitski and Milliman, 2007) and then it uses the Psi model (Morehead et al., 2003) to
 430 compute daily data. In the version presented by Cohen et al. (2014) the floodplains were
 431 represented as temporary (final) storage areas for water (sediment). It means that the flows reach
 432 the floodplains when the bankfull discharge is exceeded, and water can return to the river when
 433 discharge is below bankfull.

434 The *Diff*(%) was also used for the comparisons between MGB-SED AS and WBMsed outputs
 435 in 51 sites (see Table S2 and Figure S2, Supporting Information). The WBMsed grid cells
 436 identification was performed manually, and the selected sites are the same as the in-situ stations
 437 used for the comparisons against regional studies, which enable contrasts between scales and
 438 studies. Long-term average QSS were computed with both models in the period 1993-2009. The
 439 WBMsed outputs can be obtained at <https://sdml.ua.edu/datasets-2/datasets/>.

440 3.4.2 Analysis of Sediment Flows in South America

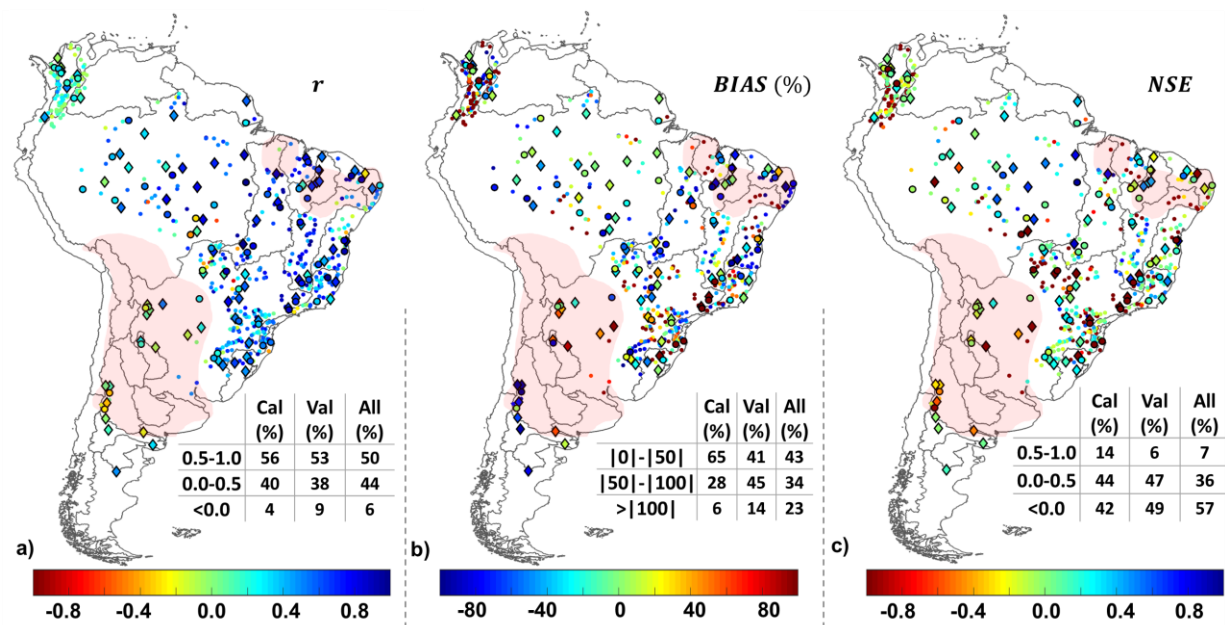
441 A study of QSS patterns was conducted using time series, from the calibrated model. QSS were
 442 simulated using the inertial and Muskingum-Cunge routing methods to assess the impact of
 443 fluvial hydrodynamics and floodplains on sediment transport and deposition. We also evaluate
 444 the effect of calibration and hydrodynamic routing on sediment delivery to the Oceans. For this
 445 purpose, we compared the estimated loads from a simulation considering hydrodynamic routing
 446 without calibration (i.e., setting the values 11.8 and 0.56 for parameters α and β , respectively)
 447 versus simulations using the inertial and Muskingum-Cunge methods to estimated loads
 448 considering the calibrated model.

449 To understand the spatial dynamics of the sediment flows in the SA, long-term averages of SSC,
 450 denudation rate, deposition of suspended sediment in the floodplains, and water discharge were
 451 calculated. We identified the major floodplains where the highest deposition rates occur, but the
 452 results were only presented for those basins where the model was calibrated, i.e., where there
 453 was no transfer of parameters, as in the case of the Orinoco River basin. We also computed the
 454 annual sediment balance at the outlets of the large rivers and for the whole SA.

455 **4 Results and Discussions**456 **4.1 Model Validation**457 **4.1.1 Simulated data vs. in-situ observations**

458 The mass balance analysis (Table S3, Supporting Information) showed that the MGB-SED AS
 459 model remained stable throughout the simulation. Numerical errors were of the $10^{-2}\%$ order,
 460 mostly coming from variables truncation in the operations.

461 The simulated QSS was compared against observed daily values, and the performance of the
 462 model was evaluated in Figure 4 in terms of r , $BIAS$ and NSE . Other metrics are shown in
 463 Figure S3 of the Supporting Information. The better performance is found in the Amazon,
 464 Tocantins, São Francisco and Doce basins.



465

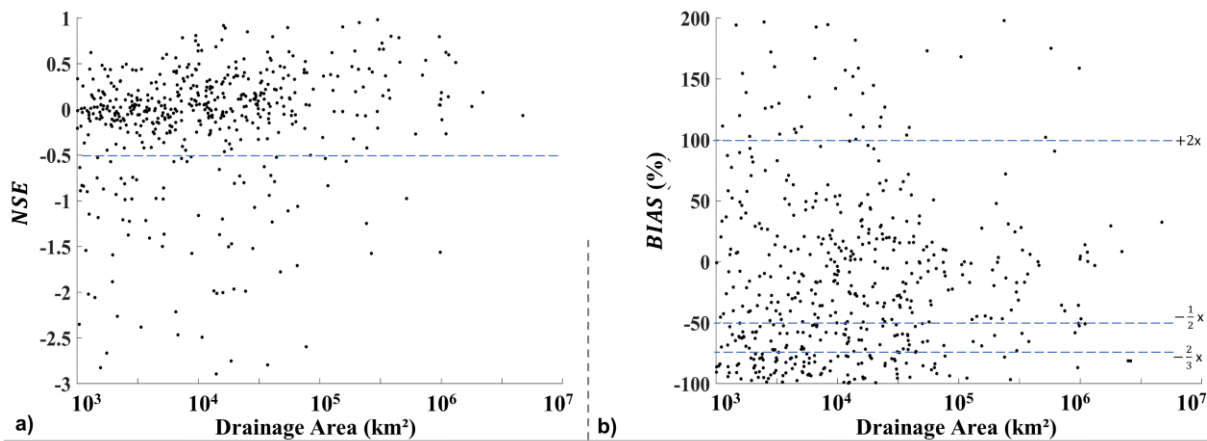
466 **Figure 4:** MGB-SED AS performance over South America in terms of suspended sediment discharge: a) correlation
 467 (r); b) $BIAS$ (%); and c) Nash-Sutcliffe efficiency (NSE). Diamonds and bigger dots refer to stations used in
 468 calibrating (Cal) and validating (Val) steps, respectively. Small dots refer to other station used to evaluate the model.

469 Tables summarize the percentage of sediment stations in each performance class and corresponding step. Marked
 470 regions represent those with poor hydrological-hydrodynamic performance (see Siqueira et al., 2018).

471 Figure 4-a indicated agreement between model estimates and observed data in terms of
 472 correlation, in which 56% and 53% of the stations had values higher than 0.5 in the calibration
 473 (Cal) and validation (Val) steps, respectively. In terms of $BIAS$, 94% (Cal) and 86% (Val) of the
 474 stations had values between -100% and 100% (Figure 4-b). For NSE , 58% and 53% of the
 475 stations had positive values (Figure 4-c). Some underestimates (negative $BIAS$) can be due to
 476 high rates of sands in suspension, as pointed by Santini et al. (2019) for the upper areas of
 477 Amazon basin. According to the authors, these rates tend to decrease from upstream to
 478 downstream. Detailed views of regions having high density of stations are shown in Figures S4,
 479 S5 and S6 (Supporting Information).

480 In the evaluation using all stations (All), Figure 4 shows that MGB-SED AS model had a
 481 lower performance in comparison to calibration. We observed a better model performance to

482 simulate QSS for stations used in the calibration, and worse model performance (r , $NSE < 0.0$ and
 483 $BIAS > |100$) was noticed especially in three situations. The first one is related to the regions
 484 where the hydrological model performed poorly (Figure 4), characterized by arid or semi-arid
 485 climate; regions where snow melting plays an important role for the runoff generation; and
 486 regions influenced by orography (Siqueira et al., 2018). The second one is represented by rivers
 487 influenced by the presence of dams, which affect the sediment transport, such as the São
 488 Francisco, Jequitinhonha, Tocantins, Paraná, Salado, Madeira, Parnaíba and Doce rivers (See
 489 Figure 1 and Figure 4). The third one is for the stations having small drainage areas. For the
 490 latter situation, Figure 5 presents a detailed description of the modeling results that relate the
 491 drainage area of each station to the NSE and $BIAS$ values. It is noted that for areas larger than
 492 $100,000\text{km}^2$, the $BIAS$ range is reduced (values between -67% and 200%), remaining mostly
 493 between -50 and 50% (Figure 5-b). For the NSE , most values are over -0.5 (Figure 5-a). Basins
 494 draining small Andean areas are very susceptible to landslides, delivering a large amount of
 495 sediments to the rivers (Restrepo et al., 2006; Martín-Vide et al., 2014). As mentioned before,
 496 MGB-SED AS does not explicitly represent landslide processes, showing low performance in
 497 these areas (e.g. headwaters of Magdalena, Bermejo and Pilcomayo rivers).



498

499 **Figure 5:** NSE and $BIAS$ (%) between observed and simulated QSS compared against the drainage area.
 500 Dashed blue lines in b) represent how much MGB-SED AS model over or underestimate QSS values.

501 Many stations that have small drainage areas are found in Colombia, for example. The results of
 502 Figure 4 in this region do not show a specific pattern, and the NSE and $BIAS$ values are
 503 sometimes negative, sometimes positive (see Figures S5, S6 and S7, Supporting Information).
 504 These basins also have high slope values and are characterized by the occurrence of strong
 505 storms (Restrepo et al., 2006). Also, sediment data from IDEAM are estimated by using a
 506 relationship between surface measurements and cross section measurements. This can be a
 507 source of uncertainties that must be taken into account when interpreting the results. The
 508 resolution of the models input data and the computational resources generally available make it
 509 difficult to represent these features in continental-scale models.

510 In Table S5 of the Supporting Information, we present an analysis of the model performance for
 511 several stations and the period when the model was calibrated (2002-2009) and the non-
 512 calibrated (1992-2001). The analysis shows that temporal extrapolation performed better than
 513 spatial extrapolation. The temporal extrapolation refers to the model evaluation for calibrated
 514 stations in another period. Spatial extrapolation refers to the model evaluation in the same period
 515 as the calibration, but for stations not used in that process.

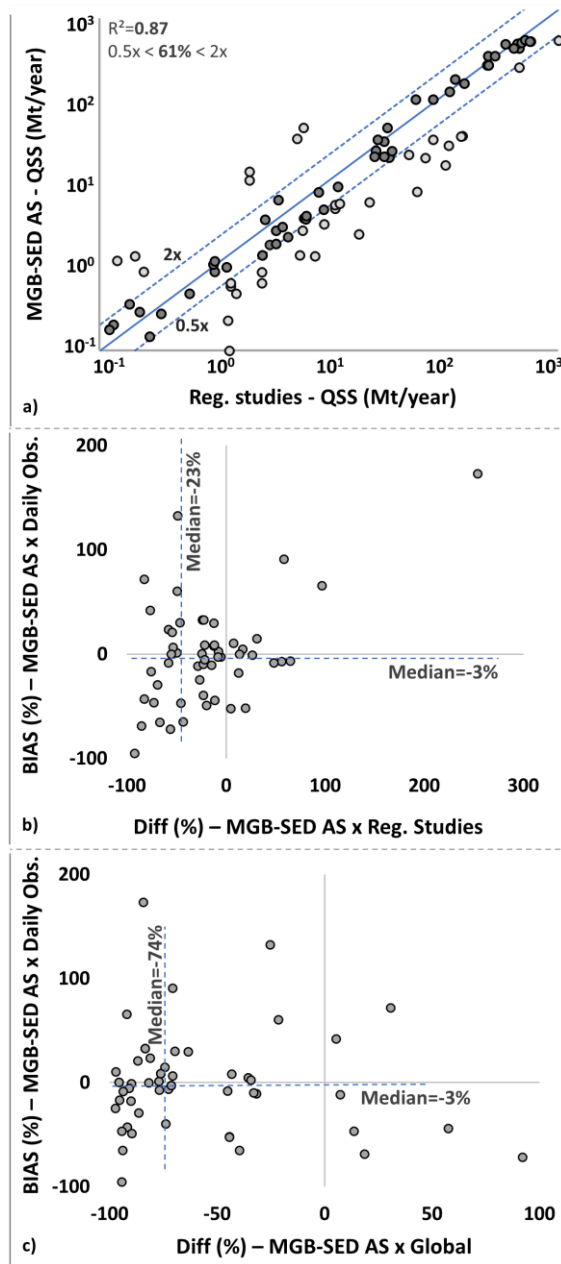
516 4.1.2 Simulated data vs. other studies

517 The comparison between simulated annual QSS and estimated annual QSS by regional
518 studies showed an $R^2=0.87$ (Figure 6-a). 61% of comparisons revealed that the MGB-SED AS
519 estimates range between half and twice the values found in regional studies.

520 Figure 6-a also shows a trend for MGB-SED AS QSS to be lower than the regional
521 studies QSS. Figure 6-b presents a comparison of *BIAS* (MGB-SED SA and in-situ measured
522 data) versus *Diff* (MGB-SED SA and regional studies). The results indicate that the *BIAS* and
523 *Diff* median were, respectively, -3% and -23%.

524 To understand the differences presented in the previous paragraph, we highlight that: i)
525 the medians of *BIAS* and *NSE* were, respectively, -3% and 0.11 for the 49 analyzed stations; ii)
526 in the Altamira station, for example, the daily *BIAS* and *NSE* were, respectively, 0% and 0.78,
527 but in comparison with Filizola and Guyot (2009) study, the MGB-SED AS has estimated for this
528 station QSS values 55% lower; iii) the regional studies (Table S1, Supporting Information)
529 provided estimates using regression methods between QSS and water discharges. From the three
530 points presented, we realize that MGB-SED AS had better agreement with in-situ data (for the
531 most comparisons) than with estimated data from regional studies. Besides, the regression
532 methods used in the aforementioned studies are simplified, and they consider some assumptions
533 that may increase their estimates, such as: the use of few in-situ measured data, in which the
534 majority belonging to the low-concentration period, to represent the temporal dynamics of
535 sediments; Q enough to explain QSS; the increase of QSS is always increasing with Q. However,
536 because of hysteresis effects, it is known that these premises often do not occur in nature,
537 especially for large rivers, which is clearly demonstrated for the Amazon in studies performed by
538 Bourgoin et al. (2007), Filizola et al. (2011) e Fassoni-Andrade and Paiva (2019). A broader
539 discussion on this topic is presented in the next section.

540 The worst performance of MGB-SED AS was at Javari station (ID=45, Figure S2 and
541 Table S1 - Supporting Information), where *BIAS* and *Diff* were, respectively, -95% and 92%.
542 Javari station has a drainage area closer to 1×10^4 km² and the model calibration in the same sub-
543 basin was performed by having focus on Solimões station (ID=47, Figure S2 - Supporting
544 Information), which has a drainage area closer to 1×10^6 km². Situations like this show the
545 difficulty to achieve a model with high performance to estimate daily QSS for all the continental
546 domain and why the model has a better performance for stations with larger drainage areas
547 (Figure 5).



548

549 **Figure 6:** Performance of the MGB-SED AS model against in-situ observations, the results of regional and global
 550 studies. a) comparison between MGB-SED AS annual suspended sediment discharge (QSS) and QSS from regional
 551 studies; light gray dots refer to when the MGB-SED AS estimated more than double or less than half the regional
 552 studies values. b) comparison between daily simulated (MGB-SED AS) and observed (in-situ) QSS (*BIAS*) against
 553 annual simulated QSS (MGB-SED AS), and estimated from regional studies (*Diff*). c) comparison between daily
 554 simulated (MGB-SED AS) and observed (in-situ) QSS against annual simulated QSS from MGB-SED AS, and from
 555 the WBMsed global model (Cohen et al., 2014), using *BIAS* and *Diff*, respectively. In figure b) (c): a point exactly
 556 at the origin $(x,y)=(0,0)$ means that both the results simulated by MGB-SED AS and those from regional
 557 studies (global model) have strong agreement with the in-situ observations; the point $(x,y)=(-100,-100)$ means that the
 558 MGB-SED AS model had a poor performance compared to the observed data and a worse performance than the
 559 results of the regional studies (global model); the point $(x,y)=(-100,0)$ means that the MGB-SED AS model
 560 performed better, if compared to the observed data, than the values estimated by regional studies (global model).

561

562 Figure 6-c presents a comparison between the results of MGB-SED AS and those of the
 563 WBMsed global model (Cohen et al., 2014). The median *Diff* between the MGB-SED AS and
 564 the WBMsed model was -74%. It shows that the estimated values by MGB-SED SA are
 565 considerably lower than those predicted by WBMsed. In this case, although the WBMsed model
 566 does not consider only Q to estimate QSS, it is based on a global empirical equation, which may
 567 have limitations given the different variables around the globe.

568 After an analysis of Figure S2 and Table S2 (Supporting Information), no spatial pattern
 569 of the *Diff* metric was found. WBMsed showed a tendency to overestimate both MGB-SED AS
 570 and in-situ measurements. This can be related to several aspects, like: i) differences in
 571 precipitation grids used by the models and their associated resolution; ii) differences in
 572 computing slopes, which can greatly affect the erosion rates (Garcia-Ruíz et al. 2015); iii)
 573 Muskingum-Cunge method to route the flow, which is not suitable to represent backwater and
 574 floodplain effects for several South America regions (e.g. Angarita et al., 2018; Bravo et al.,
 575 2012; Paiva et al., 2013, 2011; Pontes et al., 2017; Siqueira et al., 2018; Zhao et al., 2017) ; and
 576 iv) the QSS estimated by the WBMsed model was neither calibrated nor validated by Cohen et
 577 al. (2014) in SA. However, it is worth mentioning that the complexity of the WBMsed makes it
 578 difficult to accurately compare the factors that impact sediment estimates.

579

580 The tables used to generate Figure 6 graphics can be found on the Supporting Information
 581 (Table S1 and Table S2).

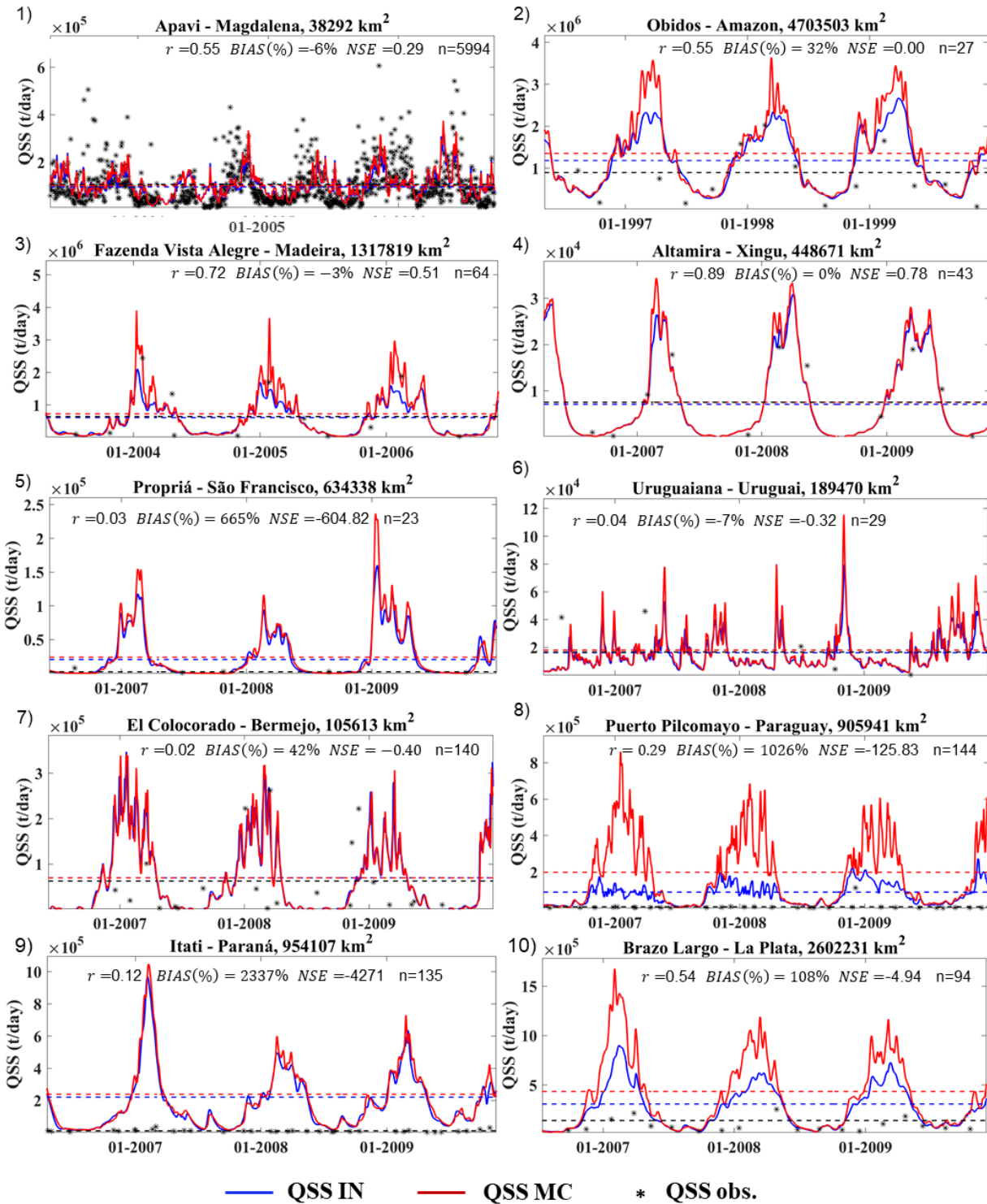
582 4.2 Analysis of Sediment Flows in South America

583 4.2.1 Time Series

584 Figure 7 presents the comparison between daily simulated and in-situ QSS data for
 585 several large South American rivers. The presented statistics were calculated considering only
 586 the values of observation dates. Apavi station, on the Magdalena river (Figure 7-1), offers a lot
 587 of observed data, and, in general, there was an agreement between the simulated and observed
 588 data ($BIAS=-6\%$ and $NSE=0.29$). In the Amazon basin, suspended sediments were well
 589 represented for several stations, which can be seen in the Fazenda Vista Alegre (Figure 7-3) and
 590 Altamira (Figure 7-3) stations. The latter had $BIAS=0\%$ and $NSE=0.78$. Óbidos station (Figure
 591 7-2) show a $BIAS$ of 30%, while upstream station showed values closer to 0% (Figure 4-b).
 592 According to Filizola and Guyot, (2009), Óbidos station has a particular protocol, where
 593 sampling is taken only in the surface zone, underestimating the real concentration (Bouchez et
 594 al.,2011). This explain why Óbidos station has a $BIAS$ value in disagreement with their upstream
 595 stations. It is pointed out that the variability of the QSS estimated by the sediment model is
 596 strongly influenced by the variability of hydrological variables calculated by MGB AS (see
 597 Equation 1).

598 The impact of fluvial hydrodynamics on sediment transport can be observed at Fazenda
 599 Vista Alegre, Óbidos, Puerto Pilcomayo (Figure 7-8) and Brazo Largo (Figure 7-10) stations,
 600 where backwater effects and floodplain storage reduce the sediment transport by 16%, 13%,
 601 55%, and 30%, respectively. In other places like Altamira (Figure 7-4) and Paraná (Figure 7-9)
 602 stations, sediment transport was reduced by 6%. These are regions where rivers generally have

603 higher slopes and the effect of floodplains is less expressive. 36% of simulated river reaches
 604 showed sediment storage in floodplains greater than 1 t/year. More information about the
 605 importance of floodplains are presented in the next sections.



606

607 **Figure 7:** Comparison between observed (QSSObs - black asterisks) and simulated suspended sediment discharge
 608 (QSS) for some large rivers of South America. Model performance is presented in terms of correlation (r),

609 *BIAS* (%) and Nash-Sutcliffe efficiency (*NSE*) for hydrodynamic modeling (QSS IN). Daily QSS simulated time
 610 series are presented for both inertial (QSS IN - blue lines) and Muskingum-Cunge (QSS MC – red lines) routing
 611 methods. Dashed lines show the respective long term averages. *n* is the number of observed QSS. The sediment
 612 stations locations are presented in Figure 8-a.

613 In the Propriá station, the *BIAS* was 665%, and in-situ QSS values were always very low
 614 (Figure 7-5). In this case, as for other stations like Paraná (*BIAS* 2337%, Figure 7-9), these low
 615 observed values are associated with sediment trap in large dams located upstream. Highlighting
 616 this phenomenon is important because, in these cases, the observed temporal dynamics are
 617 inconsistent with the simulated natural sediment discharge in the rivers.

618 The Puerto Pilcomayo station (Figure 7-8), in the Paraguay River, also showed low
 619 performance, which can be related to the difficulty of the MGB AS model to represent the strong
 620 deposition that occur in the Pilcomayo River (upstream the Pilcomayo, *BIAS* has negative
 621 value). Due it and large impoundments in the Paraná River, MGB-SED AS overestimate the
 622 observed values of QSS in the outlet of the La Plata River (Figure 7-10)

623 In many places, the model estimates and in-situ observations did not match, which may
 624 have been caused by the non-representation of reservoirs in the modeling process. In the São
 625 Francisco River, sediment trapped by reservoirs may approach 70% (Creech et al., 2015).
 626 Syvitski et al. (2005), considering impoundments, estimated that sediment flows to the oceans in
 627 SA were reduced by about 13%/ year. The expectation of the construction of new dams in the SA
 628 and their impacts on water and sediment flows, mainly in the Amazon Basin (Latrubesse et al.,
 629 2017), have grown. Besides, studies like Dunn et al.(2018) and Dunn et al. (2019) have shown
 630 the importance of quantifying sediment flows in the present and future scenarios because large
 631 and important rivers around the world have stopped supplying their deltas.

632 Figures S8, S9 and S10 show the number of QSS observed data for each sediment station.

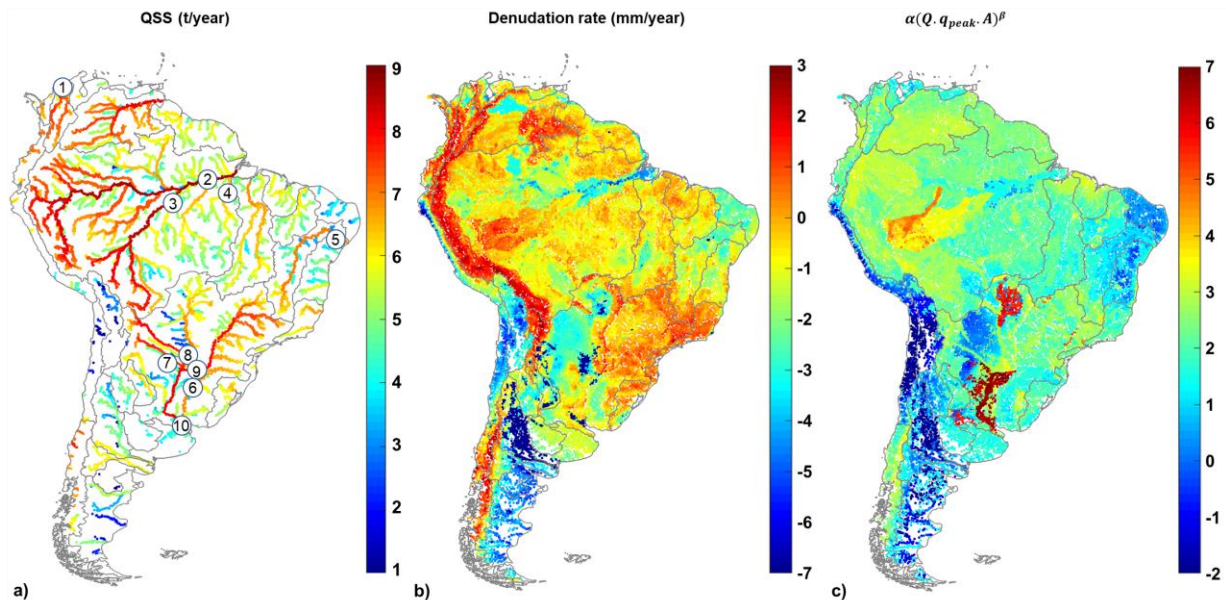
633 4.2.2 Spatial Analysis

634 Figure 8-a presents the long-term average annual QSS (t/year). From the simulated
 635 results, the Amazon River is the one with the highest QSS (4.36×10^8 t/year), followed by the
 636 Orinoco (1.37×10^8 t/year), La Plata (1.11×10^8 t/year) and Magdalena (3.26×10^7 t/year) rivers.
 637 The Magdalena carries a load for times greater than those carried by the São Francisco (7.46×10^6
 638 t/year) and Tocantins (7.44×10^6 t/year) rivers, which have twice their drainage area. The average
 639 flows of the São Francisco and Tocantins rivers are 56% lower and 88% higher, respectively,
 640 than the Magdalena river. The Doce River transports a suspended load of 5.04×10^6 t/year, which
 641 is equivalent to 70% of the load carried by the Tocantins River, although the Doce River has a
 642 drainage area (flow) ten (fourteen) times smaller.

643 Andean rivers flowing to Pacific Ocean also exhibit high rates of sediment transport
 644 (QSS $\sim 10^7$ t/year), except for dry regions like in the northern Chile. These Andean rivers show
 645 QSS values in the same order of São Francisco and Tocantins rivers (Figure 8-a), which places
 646 them among the main sediment transporters of the SA, although they drain a considerably
 647 smaller area.

648 The simulated QSS for the most downstream stations of each basin agreed with the
 649 observed values (*BIAS* values, Figure 4). Figure 8-a represents a natural potential transport
 650 situation in the rivers, since a sediment trapping in dams was not considered in the sediment
 651 modeling. Rivers such as the São Francisco and Paraná, for example, currently have field clearer

652 waters downstream from the dams in comparison to what is suggested by the sediment
 653 simulation.



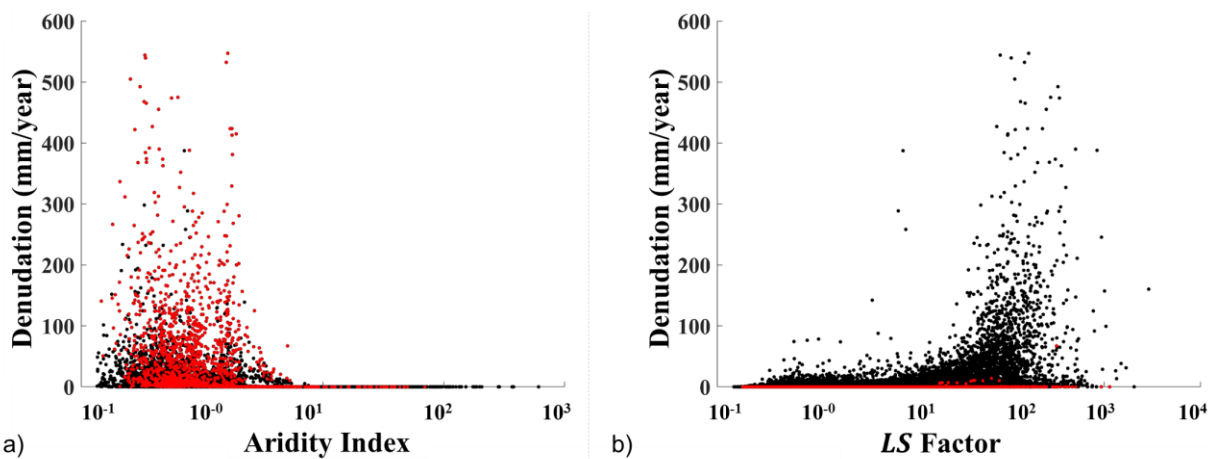
654
 655 **Figure 8:** Average Annual a) suspended sediment discharge (QSS) over South America; b) denudation rate
 656 (silt+clay+sand); and c) $\alpha(Q \cdot q_{peak} \cdot A)^\beta$. Colorbar values are in the logarithmic scale. Numbers in c) refer to
 657 stations showed in Figure 7.

658 Figure 8-b shows spatial patterns of denudation rates (soil loss in mm/year; sediment
 659 density equal to 2.65 t/m³ was used for the unit conversion, see Morris and Fan, 1998). The SA
 660 average value is 4.6 mm/year. With 16.62 mm/year, the Magdalena basin presented the highest
 661 mean denudation rate. The Amazon basin had the second-highest denudation rate of 6.8
 662 mm/year. In the Solimões, Madeira and Juruá river basins, denudation rate was 16.15, 9.89 and
 663 5.03 mm/year, respectively. For the Negro, Tapajós and Xingu watersheds, these values were
 664 0.41, 0.40 and 0.28, respectively.

665 The high denudation rates calculated for the Magdalena and Amazon river basins are
 666 mainly associated with the high slopes and strong storm events in the Andean region (see Guyot
 667 et al., 1996; Restrepo et al., 2006). The Restrepo et al. (2006) analysis, between 1986 and 1996
 668 using more than 30 stations, indicated an increasing trend of erosion in the Magdalena basin.
 669 Among the causes for this increase are catchments with small drainage areas having high relief
 670 and narrow alluvial plains, heavy precipitations, and changes in land use and land cover.
 671 Furthermore, compared to the Amazon, the Magdalena basin is more influenced by the Andes
 672 and has fewer flat regions (Figure 1). Paraguay (7.48 mm/year) and Orinoco (5.71 mm/year) also
 673 have high denudation rate values.

674 The Paraíba do Sul, Doce and the Paraná river basins also stand out with high denudation
 675 rates: 5.34 mm/year, 2.12 mm/year and 3.52 mm/year, respectively. These basins have a strongly
 676 undulating and hilly relief, soils covered mainly by agriculture and degraded pastures, and a very
 677 seasonal rainfall pattern, with heavy rainfall for the November-January period. Despite the
 678 Paraíba and São Francisco river basins having a hilly relief, they are in a semi-arid region, for
 679 which lower denudation rates are estimated (0.28 mm/year and 0.85 mm/year, respectively).

680 The relations between denudation rate, slope (represented by the *LS* factor), and
 681 precipitation (represented by the Aridity index) are presented in Figure 9. Red dots in Figure 9-a
 682 and Figure 9-b, correspond to rivers for which the *LS* factor and Aridity Index are above the
 683 percentile 95%, respectively, which indicate steeper (Figure 9-a), and extremely dry (Figure 9-b)
 684 areas. This figure shows, in agreement with Figure 3 and Figure 8, that high denudation rates
 685 can occur for high and low slopes, and are found mainly in humid areas (Aridity Index <100,
 686 Figure 9-a), while arid regions always have very low denudation rates (Figure 9-b). Figure 9
 687 shows that a pattern between the denudation rate, *LS* factor and aridity index does not exist. We
 688 expected this, since the model considers several processes based on what occurs in nature, and
 689 not only the water discharge, to estimate erosion and sediment transport. García-Ruiz et al.
 690 (2015) identified, from several studies around the world, that almost all erosion rates can occur
 691 for any climate condition. The authors also pointed out that a significant effect of the increase in
 692 erosion rates occurs as precipitation and slope rise. This increase tends to reach, on average, a
 693 limit when the slope and precipitation reach $\pm 0.2\text{m/m}$ and $\pm 1,400\text{mm/year}$, respectively.



694
 695 **Figure 9:** Denudation rate versus: a) Aridity Index (red dots represent *LS* values above the percentile 95%); b) *LS*
 696 factor (red dots represent Aridity Index values above the percentile 95%).

697 The MUSLE factor related to the ability to remove soil particles is the $\alpha(Q \cdot q_{peak} \cdot A)\beta$.
 698 In regions such as Brazilian northeast, Chaco, Atacama Desert, and others in the south of the
 699 continent (Desaguadero, Colorado and Negro river basins), the values of this factor are
 700 comparatively low concerning the rest of the SA. High values are found in the Pantanal, Purus
 701 River basin, part of the Juruá River basin, and in the lower La Plata river basin (Figure 8-c). It is
 702 noticeable that some spatial patterns presented in Figure 8-b are directly related to the standards
 703 presented in Figure 8-c, showing the influence of the $\alpha(Q \cdot q_{peak} \cdot A)\beta$ factor in the denudation
 704 rate.

705 In the Pantanal, Juruá River and Purus River, even the $\alpha(Q \cdot q_{peak} \cdot A)\beta$ factor values
 706 being higher, the simulated QSS tended to underestimate the observed values (Figure 4). Thus,
 707 we believe that these highlighted values may be related to the calibration parameters of the
 708 hydrological model and the spatial discretization performed by Siqueira et al. (2018), which was
 709 more focused on hydrological processes than sediment processes. Also, no pattern was observed
 710 in the maps of the input parameters (Figure 3) that could explain the observed pattern for the
 711 Purus and Juruá river basins in Figure 8-b. The high values in the La Plata river basin may be
 712 associated with large wetlands, which produces high runoff but low sediment yield.

713 4.2.3 Multiple relationships: water discharge, sediment concentration and deposition

714 4.2.3.1 Overview

715 Figure 10 shows SA rivers with the highest Q and SSC values according to the modeling
716 results. The figure illustrates that largest SSC values in the Amazon basin are located in the
717 upper Madeira River and other rivers having the headwaters in Andean regions, as already
718 known by previous studies (Amsler and Drago, 2009; Cohen et al., 2014; Latrubesse et al.,
719 2005). The pattern found in the river reaches with higher and lower concentrations in the central
720 Amazon matches well with the results found by Fassoni-Andrade and Paiva (2019) using remote
721 sensing. The greatest differences are found downstream of the confluence between the Amazon
722 and Tapajós rivers, where the SSC (Figure 10) keeps decreasing, while Fassoni-Andrade and
723 Paiva (2019) observed an increase downstream of the confluence with the Xingú River. The
724 authors concluded that this difference could be associated with sediment resuspension caused by
725 variations at the Amazon estuary, which are not represented in the MGB-SED AS model.

726 The Magdalena, Bermejo, Pilcomayo, and some rivers in the south of SA showed high
727 concentrations. The Amazonian rivers without headwaters in the Andes have low SSC, such as
728 the Negro, Tapajós and Xingu rivers (Figure 10), having high water discharge values (>9,700
729 m³/s in average, see Filizola and Guyot, 2009).

730 According to MGB-SED AS simulations, 2×10^9 t/year of silt and clay leave the hillsides
731 and reach the SA rivers. Of these, about 12% are trapped in the floodplains before reaching the
732 Oceans under natural conditions (i.e., without impoundments). This value can be substantially
733 higher for some regions. As related by Bourgoïn et al. (2007) and most recently by Rudorff et al.
734 (2018), the mean trap efficiency for the floodbasin encompassing the Lago Grande de Curuai
735 (lower Amazon River) is 45%-48%. For this region, strong winds can induce waves
736 resuspending fine sediment in dry seasons, when the floodplains and lakes are shallow (Bourgoïn
737 et al., 2007; Fassoni-Andrade and Paiva, 2019a; Schmidt, 1972), which means that less sediment
738 is trapped. Despite the importance of the wind effect for this region, it was not considered in the
739 current study. Meanwhile, for the central Amazon floodplains, the trapped value found is one
740 order ($\sim 10^7$ t/year) bigger than that estimated by Rudorff et al. (2018) only for one reach. It is not
741 possible to make a direct comparison due to the different approaches used in the aforementioned
742 studies.

743 The effect of SS deposition on the floodplains is quite evident in the highlands of
744 Madeira river basin (Figure 10), causing a sharp reduction in SSC values from upstream to
745 downstream. For example, Guyot et al. (1996), using regressions between observed Q and QSS
746 data, estimated a reduction for QSS and SSC of 54% and 95%, respectively in the Mamoré basin.
747 In comparison, we estimated a 35% (75%) increase (decrease) in QSS (SSC). As discussed in
748 section 4.1.2, the main differences can be associated to the methods used to estimate QSS values
749 (regression analysis \times sediment modeling), which may be enough to find such different results
750 and patterns.

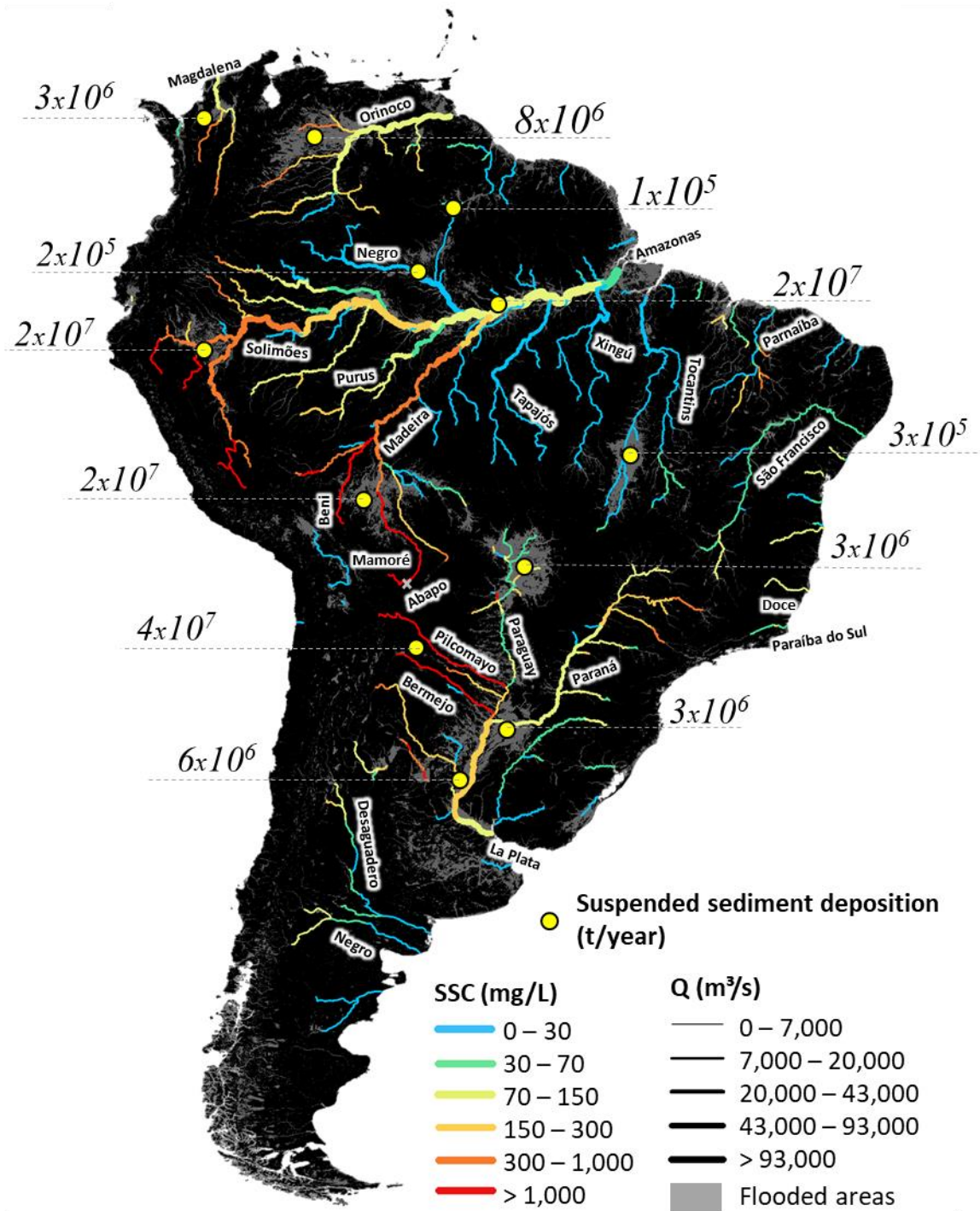
751 The region assessed on the Mamoré River drains a large amount of sediment originating
752 in the Andes. The same happens with the Pilcomayo River. The Mamoré River flows through
753 regions with dynamic and complex fluvial geomorphology, with avulsion and silting
754 mechanisms of the bed in the Llanos de Moxos floodplain. According to MGB-SED AS
755 simulations, $\sim 2 \times 10^7$ t/year of SS are deposited in this floodplain (Figure 10). The Pilcomayo

756 River flows through and floods the flat regions of the Chaco, losing water to the atmosphere
757 through evapotranspiration (Martín-Vide et al., 2014). The Pilcomayo River basin also presents
758 great complexities, similar to those described for the Mamoré River (see Martín-Vide et al.,
759 2014). In the upper Pilcomayo, near the Andes, Martín-Vide et al. (2014) estimated a mean SSC
760 of $15 \times 10^3 \text{mg/L}$, while SCC simulated was $28 \times 10^3 \text{mg/L}$. For Pilcomayo station, Martín-Vide et
761 al. (2014) estimate a QSS of 140 Mt/year, while for the same station (*BIAS*=-20% and
762 *NSE*=0.23), MGB-SED AS estimate was 96 Mt/year. Guyot et al. (1996) estimated a mean SSC
763 of $13 \times 10^3 \text{mg/L}$ in Abapo (Figure 10), about two times higher than estimated by MGB-SED AS
764 ($6 \times 10^3 \text{mg/L}$) and by Buarque (2015), in which it was found $5 \times 10^3 \text{mg/L}$ (personal
765 communication) using a regional model.

766

767

768



769

770 **Figure 10:** Annual average of suspended sediment load deposited in the main floodplains of South America; long-
 771 term daily average of suspended sediment concentration (SSC) and water discharge (Q) for main large rivers.
 772 Flooded areas were acquired from Fluet-Chouinard et al. (2015).

773 MGB-SED SA has estimated lower SSC values in the Mamoré River when compared to
 774 Guyot et al. (1996) estimates. The main differences found could be related to the following
 775 aspects: i) there was difficulty in calibrating the continental-scale model in the regions of upper
 776 Madeira, with the available data; ii) the processes observed in the Andean region, such as

777 landslide-driven sediment flux, are not well represented in the proposed modeling as discussed
 778 by Buarque (2015), which shows that significant uncertainties for these regions may exist. The
 779 same can occur for other Andes regions, like the headwater of the Pilcomayo, Bermejo and
 780 Magdalena rivers.

781 The Pilcomayo River was the only river that showed an increase in concentrations from
 782 upstream to downstream (Figure 10). It happens because simulated Q values increase from the
 783 upstream to the middle Pilcomayo and decrease again next to the outlet. Martín-Vide et al.
 784 (2014) noted that the increase in Q is not proportional to the SSC for the Pilcomayo River. This
 785 behavior was identified using MGB-SED AS for the Mamoré River, which differs from the
 786 approach used by Guyot et al. (1996). Using the MGB-SED model, which considers several
 787 processes and variables and not only Q to estimate the QSS, Buarque (2015) found a $NSE=0.7$
 788 in the Fazenda Vista Alegre station (Madeira River). This indicates that the connection suggested
 789 in some studies (e.g. Filizola and Guyot, 2009; Guyot et al., 1996; Lima et al., 2005; Meade et
 790 al., 1990; Restrepo et al., 2006), that QSS always increases with Q, cannot always be applied.

791 The assessment in large flooded areas (Figure 10) indicated that 57% of the total SS
 792 trapped in the floodplains is deposited in these places. The plains having the highest amounts of
 793 deposited SS are the Banãdo La Estrella (4×10^7 t/year), Llanos de Moxos (2×10^7 t/year), central
 794 Amazon floodplains (2×10^7 t/year) and the interfluvial floodplains of Peru (2×10^7 t/year). In the
 795 whole Amazon basin, about 1×10^8 t/year of SS are deposited in floodplains, which corresponds
 796 to ~50% of total SS trapped in the floodplains in the whole South America.

797 4.2.3.2 Annual Sediment Balance

798 The impact of model calibration and hydrodynamic routing in South America was also
 799 assessed by the suspended loads leaving the continent. When using the hydrodynamic model
 800 without calibration, the QSS reaching the oceans was 2.86×10^9 t/year. After calibration, this
 801 value was 1.00×10^9 t/year, which means that the calibration of MGB-SED AS provided
 802 estimates 65% lower. When the calibration and Muskingum-Cunge routing method were
 803 considered, the value increased by 18% (1.18×10^9 t/year). Syvitski et al. (2005) estimated for
 804 "prehuman" period that QSS delivered from SA was, on average 2.68×10^9 t/year, a value 268%
 805 (6%) higher (lower) than estimated with calibrated (non-calibrated) MGB-SED AS. In their
 806 global study on tropical rivers, Syvitski et al. (2014) highlighted that most modeling projects use
 807 boundary conditions without considering sediment depositions in the deltas, which could reduce
 808 the value of the SS that effectively leaves the continent. In this paper, we partially represent this
 809 effect, since the model does not consider coastal basins and islands with $A < 1,000 \text{ km}^2$ or
 810 submerged coastal regions.

811 Naturally (without considering impoundments), the daily water (SS) transport of
 812 $3.10 \times 10^{10} \text{ m}^3$ (2.76×10^6 t) by the SA rivers to the oceans was estimated using MGB-SED AS. Of
 813 this total, 57% (43%) of the water (SS) volume comes from the Amazon basin.

814 Figure 11 presents a monthly balance of SS and Q for South America and several of its
 815 major rivers. In addition, to expand the understanding of the different relations between Q and
 816 SSC, a map with the Delay Index (DI) calculated between these two variables is also presented
 817 in this figure. Values in red (blue) shades show how many days the SSC peak is ahead (behind)
 818 in relation to the Q peak.

819 The *DI* map (Figure 11) shows that the occurrence of the SSC peak earlier than the Q
820 peak is mainly in some Amazon tributaries, Brazilian northeast and areas closer to Atacama
821 Desert. In the Paraná, São Francisco (Figure 11-f), Bermejo, Magdalena (Figure 11-b), Doce
822 (Figure 11-g), and Paraíba do Sul river basins, *DI* values are closer to zero. A common feature of
823 these basins is that they have hilly relief regions and relatively few flat areas, which facilitates
824 the transport of water and sediments to (and along) river channels.

825 Throughout the year, the simulated QSS in SA ranged $3-7 \times 10^7$ t/day, in which higher
826 values were occurring between February and June (Figure 11-d). The SS deposition on the
827 floodplains has higher values between November and April.

828 In the Amazon River, the sediment supply (MUSLE) peak was in January, together with
829 the floodplains deposition (Dep) peak, and the QSS peak only occurs in February (Figure 11-a).
830 The Amazon River dynamics is mainly influenced by lateral contributions, which is related to
831 the variation of the rainy periods in the south and north of the basin (Villar et al., 2008). In the
832 south, there is the Madeira River basin with high sediment yield (44% of all Amazonas) and the
833 occurrence of QSS and Q peaks, respectively, in February and April. In the north, there is the
834 Negro River with low sediment yield (1.5% of all Amazonas) and the occurrence of QSS and Q
835 peaks, respectively, in June and July. The Solimões and Madeira rivers is those one that, in fact,
836 control the temporal dynamics of the Amazon River in the outlet. In the Solimões river, the
837 discharge, sediment supply and deposition of SS occur concomitantly in March. Both SSC
838 (Figure 10) and QSS decrease from upstream to downstream in Amazon basin (Solimões-
839 Amazon rivers). The QSS and SSC back to increase from the confluence with Madeira River.

840 The Magdalena River showed two Q peaks (Figure 11-b), where the first peaks are about
841 two months apart (May-July) and the last in about one month (November-December). SS
842 (discharge, sediment supply and deposition on floodplains) also have two peaks, occurring in
843 May and in November, concomitantly with Q peaks. In the La Plata River, the Q and QSS peaks
844 were observed in March and February, respectively. The SS supply peak was observed in
845 February, and about 10% of these sediments are then deposited on floodplains, in which the
846 deposition peak occurs in January (Figure 11-c).

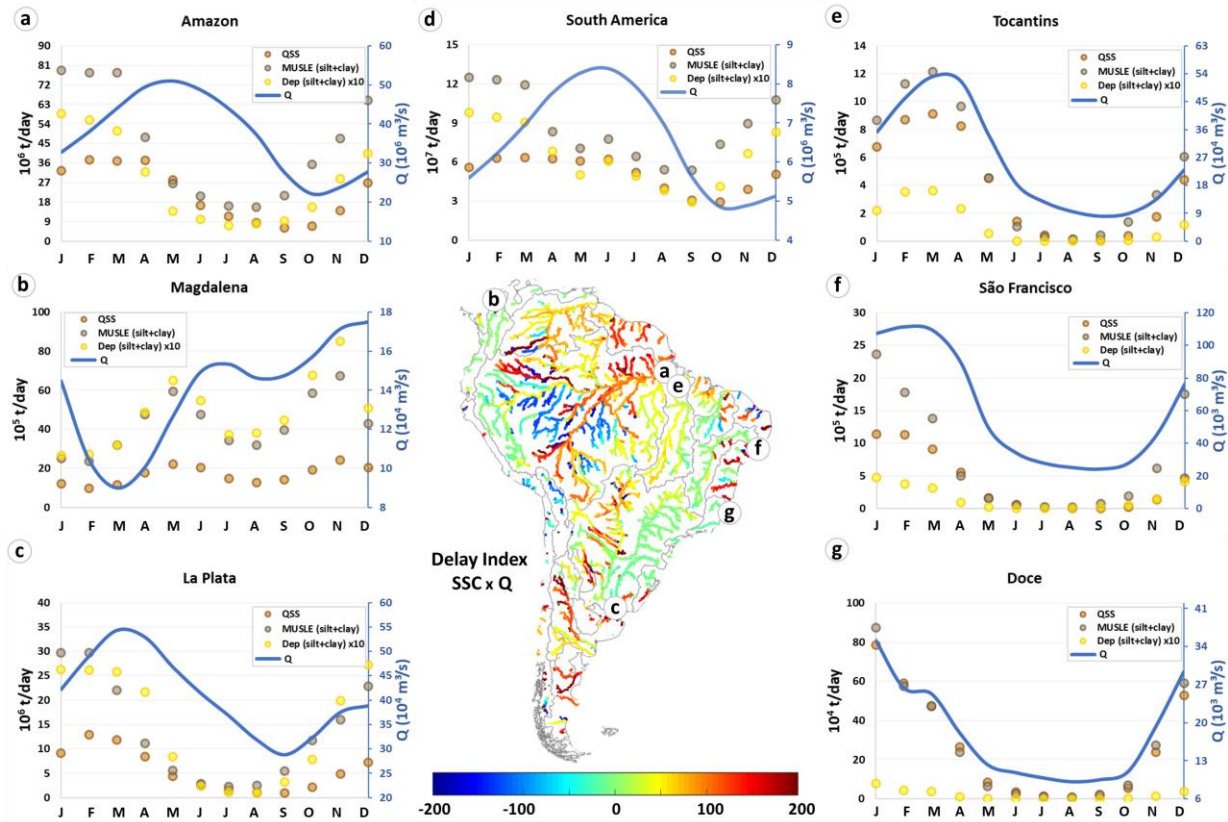


Figure 11: Annual sediment balance for South America and some large rivers. Figures a-g show water discharge (Q) in blue lines, suspended sediment load estimated with MUSLE equation in gray circles, suspended sediment discharge (QSS) in brownish circles, and suspended sediment deposited in floodplains (Dep) in yellow circles. Dep values are one order below other sediment values, so in the figure, we raised the values tenfold. The central map shows the Delay Index, calculated between the suspended sediment concentration (SSC) and Q. Reddish (blue) values show how many days the SSC peak is ahead (delayed) in relation to the Q peak.

The Tocantins (Figure 11-e) and São Francisco (Figure 11-f) river basins have a similar area, are geographic close to each other but have very different sediment flows. The Tocantins River (Figure 11-e) has a large floodplain on the Araguaia River, while the São Francisco River has almost no floodplains (Figure 1). Despite this, the São Francisco river basin has a more deposited SS load than that of Tocantins. This occurs because the São Francisco transports a larger load with lower flows, which facilitates deposition and because the Araguaia River has a lower sediment yield in its headwaters (Figure 8-a). The SS supply, floodplains deposition and transport occur in January to the São Francisco and in March to the Tocantins.

The Doce River presents a straightforward relationship between water discharge and sediments, and similar monthly variations (Figure 11-g). The Q and QSS peaks occur in January, and only about 0.6% of the sediments reaching the drainage network (this value can be zero for dry season) are deposited in floodplains.

Figure 11 shows that in basins with larger flat areas (e.g., Magdalena, Amazonas and La Plata), the SS supply peak occurs concomitantly with the deposition peak. In the Doce and São Francisco river basins, the SS supply peak occurs together with the deposition and also Q peaks. It means that only for the highest flows the SS reach the floodplains of these basins. In the

870 Tocantins river basin, this fact may be related to the low sediment transport in the Araguaia
871 River, which is the main tributary and has the largest flat regions.

872

873

874 **5 Conclusions**

875 In this research, we performed the coupling of the MGB-SED sediment model with the
876 hydrologic-hydrodynamic model of South America (MGB AS). From this coupling, the MGB-
877 SED AS was developed and assessed. Using the model results was possible to investigate and
878 understand temporal and spatial patterns of suspended sediment (SS) flows on a continental
879 scale.

880 The main conclusions related to the process of development, performance evaluation, and
881 application of the model for the comprehension of continental standards are:

- 882 • The MGB-SED AS model was able to perform accurate estimates at several sites, which
883 was evaluated against in-situ measurements. The calibration of the model parameters
884 improved the estimates of the SS flows, obtaining an export value from SA, under natural
885 conditions (without impoundments), equivalent to 65% of the values estimated without
886 calibration.
- 887 • The use of the hydrodynamic routing method enabled better SS estimates, especially the
888 simulated QSS peaks in places having floodplains. By using the simplified routing method
889 and without floodplains, estimates of annual loads have increased by 18%.
- 890 • We observed that the MGB-SED AS results agreed with in-situ observed QSS. The model
891 tends to estimate QSS values smaller than with the estimates from regional studies and the
892 global model used as comparison. The use of the continental model does not exclude the
893 use of models at regional and local scales for smaller-scale studies.
- 894 • The Amazon (4.36×10^8 t/year), Orinoco (1.37×10^8 t/year), La Plata (1.11×10^8 t/year) and
895 Magdalena (3.26×10^7) rivers presented the highest suspended sediment yield, meaning
896 44%, 14%, 11% and 3% of total South America discharges values to the ocean. Floodplains
897 play an important role by retaining about 12% (2.40×10^8 t/year) of SS carried by the rivers.
898 About 57% of the total deposition occurs in large flooded areas, for which the Banãdo La
899 Estrella (4×10^7 t/year), Llanos de Moxos (2×10^7 t/year), central Amazon floodplains
900 (2×10^7 t/year) and the interfluvial floodplains of Peru (2×10^7 t/year) representing the four
901 regions with the highest deposition rates.
- 902 • The increase in Q does not always result in an increase in SSC/QSS. Especially in rivers
903 with large floodplains, Q and SSC/QSS peaks can occur up to months apart.
- 904 • Catchments with higher slopes and higher rainfall have higher SSC, while QSS tends to be
905 higher where flows are higher.

906 Results presented in this work enabled the comprehension of the spatiotemporal dynamics of SS
907 flows in South America. Generated maps present the annual rates of denudation, transport
908 (discharge and concentration), and deposition (in the plains) of SS throughout the continent.
909 Charts of the annual sediment balance were also generated for some rivers chosen as having high
910 sediment transport. These information may be useful for other studies on a continental scale, for
911 example, related to reservoirs, fish productivity, nutrient transport, carbon balance, and other
912 studies related to ecosystem maintenance and soil conservation. Besides, this information can

913 support decision making, planning, and management of continental land use. Studies such as that
 914 of Latrubesse et al. (2017) have shown a possible increase of dams in South America in the
 915 future. Thus, to have a better knowledge of sediment fluxes in the present, it is necessary to
 916 consider these structures in sediment modeling, which is part of the continuation of this research.

917

918 **Acknowledgments**

919 The first and second authors thanks the Brazilian CNPq (*Conselho Nacional de Desenvolvimento*
 920 *Científico e Tecnológico*) for supporting this research under the Grants Number 167867/2018-0
 921 and 305636/2019-7.

922

923 Some datasets for this research are included in this paper: Siqueira et al. (2018).

924

925 In-situ data supporting this research are available in <http://www.snirh.gov.br/hidroweb/> (ANA),
 926 <http://bdhi.hidricosargentina.gob.ar/> (BDHI) and <http://www.ideam.gov.co/> (IDEAM).

927

928 **Data information**

929 Simulated Suspended Sediment Discharge for South America Rivers (MGB-SED AS) - V1.0 are
 930 available in: doi:10.17632/k7c5482fsm.1

931 **References**

- 932 Aguiar, A.P.D., Vieira, I.C.G., Assis, T.O., Dalla-Nora, E.L., Toledo, P.M., Oliveira Santos-
 933 Junior, R.A., Batistella, M., Coelho, A.S., Savaget, E.K., Aragão, L.E.O.C., Nobre, C.A.,
 934 Ometto, J.P.H., 2016. Land use change emission scenarios: Anticipating a forest transition
 935 process in the Brazilian Amazon. *Glob. Chang. Biol.* 22, 1821–1840.
 936 <https://doi.org/10.1111/gcb.13134>
- 937 Alewell, C., Borrelli, P., Meusburger, K., Panagos, P., 2019. Using the USLE: Chances,
 938 challenges and limitations of soil erosion modelling. *Int. Soil Water Conserv. Res.* 7, 203–
 939 225. <https://doi.org/10.1016/j.iswcr.2019.05.004>
- 940 Almagro, A., Oliveira, P.T.S., Nearing, M.A., Hagemann, S., 2017. Projected climate change
 941 impacts in rainfall erosivity over Brazil. *Sci. Rep.* 7, 1–12. <https://doi.org/10.1038/s41598-017-08298-y>
- 943 Almeida, R.M., Tranvik, L., Huszar, V.L.M., Sobek, S., Mendonça, R., Barros, N., Boemer, G.,
 944 Arantes, J.D., J., Roland, F., 2015. Phosphorus transport by the largest Amazon tributary
 945 (Madeira River, Brazil) and its sensitivity to precipitation and damming. *Inl. Waters* 5, 275–
 946 282.
- 947 Amsler, M., Prendes, H., 2000. El Río Paraná en su Tramo Medio, in: *Transporte de Sedimentos*
 948 *y Procesos Fluviales Asociados*. pp. 233–306.
- 949 Amsler, M.L., Drago, E.C., 2009. A review of the suspended sediment budget at the confluence
 950 of the Paraná and Paraguay Rivers. *Hydrol. Process. An Int. J.* 23, 3230–3235.
 951 <https://doi.org/10.1002/hyp>
- 952 Andreadis, K.M., Schumann, G.J.P., Pavelsky, T., 2013. A simple global river bankfull width
 953 and depth database. *Water Resouces Res.*
- 954 Angarita, H., Wickel, A.J., Sieber, J., Chavarro, J., Maldonado-Ocampo, J.A., Herrera-R, G.A.,

- 955 Delgado, J., Purkey, D., 2018. Basin-scale impacts of hydropower development on the
956 Mompós Depression wetlands, Colombia. *Hydrol. Earth Syst. Sci.* 22, 2839–2865.
957 <https://doi.org/10.5194/hess-22-2839-2018>
- 958 Aragão, L.E.O.C., 2012. The rainforest 's water pump. *Nature* 489, 217–218.
- 959 Arnold, J.G., Srinivasan, R., Muttiah, R.S., Williams, J.R., 1998. Large area hydrologic
960 modeling and assessment part I: model development. *J. Am. Water Resour. Assoc.*
961 <https://doi.org/10.1111/j.1752-1688.1998.tb05961.x>
- 962 Bates, P.D., Horritt, M.S., Fewtrell, T.J., 2010. A simple inertial formulation of the shallow
963 water equations for efficient two-dimensional flood inundation modelling. *J. Hydrol.* 387,
964 33–45. <https://doi.org/10.1016/j.jhydrol.2010.03.027>
- 965 Bates, P.D., Neal, J., Sampson, C., Smith, A., Trigg, M., 2018. Progress Toward Hyperresolution
966 Models of Global Flood Hazard. *Risk Model. Hazards Disasters* 211–232.
967 <https://doi.org/doi.org/10.1016/B978-0-12-804071-3.00009-4>
- 968 Beck, H.E., van Dijk, A.I.J.M., de Roo, A., Dutra, E., Fink, G., Orth, R., Schellekens, J., 2017.
969 Global evaluation of runoff from 10 state-of-the-art hydrological models. *Hydrol. Earth*
970 *Syst. Sci.* 21, 2881–2903.
- 971 Beighley, R.E., Gummadi, V., 2011. Developing channel and floodplain dimensions with limited
972 data: A case study in the Amazon Basin. *Earth Surf. Process. Landforms* 36, 1059–1071.
- 973 Benavidez, R., Jackson, B., Maxwell, D., Norton, K., 2018. A review of the (Revised) Universal
974 Soil Loss Equation ((R)USLE): With a view to increasing its global applicability and
975 improving soil loss estimates. *Hydrol. Earth Syst. Sci.* 22, 6059–6086.
976 <https://doi.org/10.5194/hess-22-6059-2018>
- 977 Best, J., 2019. Anthropogenic stresses on the world's big rivers. *Nat. Geosci.* 12, 7–21.
978 <https://doi.org/10.1038/s41561-018-0262-x>
- 979 Beusen, A.H.W., Dekkers, A.L.M., Bouwman, A.F., Ludwig, W., Harrison, J., 2005. Estimation
980 of global river transport of sediments and associated particulate C, N, and P. *Global*
981 *Biogeochem. Cycles* 19. <https://doi.org/10.1029/2005GB002453>
- 982 Bierkens, M.F.P., 2015. Global hydrology 2015: State, trends, and directions. *Water Resouces*
983 *Res.* 51, 4923–4947. <https://doi.org/10.1002/2015WR017173>.Received
- 984 Borrelli, P., Robinson, D.A., Fleischer, L.R., Lugato, E., Ballabio, C., Alewell, C., Meusburger,
985 K., Modugno, S., Schütt, B., Ferro, V., Bagarello, V., Oost, K. Van, Montanarella, L.,
986 Panagos, P., 2017. An assessment of the global impact of 21st century land use change on
987 soil erosion. *Nat. Commun.* 8, 1–13. <https://doi.org/10.1038/s41467-017-02142-7>
- 988 Bourgoin, L.M., Bonnet, M.P., Martinez, J.M., Kosuth, P., Cochonneau, G., Moreira-Turcq, P.,
989 Guyot, J.L., Vauchel, P., Filizola, N., Seyler, P., 2007. Temporal dynamics of water and
990 sediment exchanges between the Curuaí floodplain and the Amazon River, Brazil. *J.*
991 *Hydrol.* 335, 140–156. <https://doi.org/10.1016/j.jhydrol.2006.11.023>
- 992 Bravo, J.M., Allasia, D., Paz, a. R., Collischonn, W., Tucci, C.E.M., 2012. Coupled Hydrologic-
993 Hydraulic Modeling of the Upper Paraguay River Basin. *J. Hydrol. Eng.* 17, 635–646.
994 [https://doi.org/10.1061/\(ASCE\)HE.1943-5584.0000494](https://doi.org/10.1061/(ASCE)HE.1943-5584.0000494)
- 995 Brêda, J.P.L.F., Paiva, R.C.D., Collischonn, W., Bravo, J.M., Siqueira, V.A., Steinke, E.B., 2020.
996 Climate change impacts on South American water balance from a continental-scale
997 hydrological model driven by CMIP5 projections. *Clim. Change.*
998 <https://doi.org/10.1007/s10584-020-02667-9>
- 999 Buarque, D.C., 2015. Simulação da geração e do transporte de sedimetnos em grandes bacias:
1000 estudo de caso do rio Madeira. Universidade Federal do Rio Grande do Sul, Porto Alegre,

- 1001 Tese (Doutorado em Recursos Hídricos e Saneamento Ambiental).
1002 Campagnoli, F., 2006. The production of the sediment of the South America continent: propose
1003 of mapping of the erosion rates based on geological and geomorphological aspects. *Rev.*
1004 *Bras. Geomorfol.*
- 1005 Cohen, S., Kettner, A.J., Syvitski, J.P.M., 2014. Global suspended sediment and water discharge
1006 dynamics between 1960 and 2010: Continental trends and intra-basin sensitivity. *Glob.*
1007 *Planet. Change* 115, 44–58. <https://doi.org/10.1016/j.gloplacha.2014.01.011>
- 1008 Cohen, S., Kettner, A.J., Syvitski, J.P.M., Fekete, B.M., 2013. WBMsed, a distributed global-
1009 scale riverine sediment flux model: Model description and validation. *Comput. Geosci.* 53,
1010 80–93. <https://doi.org/10.1016/j.cageo.2011.08.011>
- 1011 Collischonn, W., Allasia, D., Da Silva, B.C., Tucci, C.E.M., 2007. The MGB-IPH model for
1012 large-scale rainfall—runoff modelling. *Hydrol. Sci. J.* 52, 878–895.
1013 <https://doi.org/10.1623/hysj.52.5.878>
- 1014 Creech, C.T., Siqueira, R.B., Selegean, J.P., Miller, C., 2015. Anthropogenic impacts to the
1015 sediment budget of São Francisco River navigation channel using SWAT. *Int. J. Agric.*
1016 *Biol. Eng.* 8, 1–20. <https://doi.org/10.3965/j.ijabe.20150803.1372>
- 1017 Dearing, J.A., Jones, R.T., 2003. Coupling temporal and spatial dimensions of global sediment
1018 flux through lake and marine sediment records. *Glob. Planet. Change* 39, 147–168.
1019 [https://doi.org/10.1016/S0921-8181\(03\)00022-5](https://doi.org/10.1016/S0921-8181(03)00022-5)
- 1020 Doetterl, S., Van Oost, K., Six, J., 2012. Towards constraining the magnitude of global
1021 agricultural sediment and soil organic carbon fluxes. *Earth Surf. Process. Landforms* 37,
1022 642–655. <https://doi.org/10.1002/esp.3198>
- 1023 Dunn, F.E., Darby, S.E., Nicholls, R.J., Cohen, S., Zarfl, C., Fekete, B.M., 2019. Projections of
1024 declining fluvial sediment delivery to major deltas worldwide in response to climate change
1025 and anthropogenic stress. *Environ. Res. Lett.* 14, 084034. [https://doi.org/10.1088/1748-](https://doi.org/10.1088/1748-9326/ab304e)
1026 [9326/ab304e](https://doi.org/10.1088/1748-9326/ab304e)
- 1027 Dunn, F.E., Nicholls, R.J., Darby, S.E., Cohen, S., Zarfl, C., Fekete, B.M., 2018. Projections of
1028 historical and 21st century fluvial sediment delivery to the Ganges-Brahmaputra-Meghna,
1029 Mahanadi, and Volta deltas. *Sci. Total Environ.* 642, 105–116.
1030 <https://doi.org/10.1016/j.scitotenv.2018.06.006>
- 1031 Fagundes, H. de O., Fan, F.M., Paiva, R.C.D., 2019. Automatic calibration of a large-scale
1032 sediment model using suspended sediment concentration, water quality, and remote sensing
1033 data. *Brazilian J. Water Resour.* 24, 1–18. [https://doi.org/10.1590/2318-](https://doi.org/10.1590/2318-0331.241920180127)
1034 [0331.241920180127](https://doi.org/10.1590/2318-0331.241920180127)
- 1035 Fagundes, H.O., Paiva, R.C.D., Fan, F.M., Buarque, D.C., Fassoni-Andrade, A.C., 2020.
1036 Sediment modeling of a large-scale basin supported by remote sensing and in-situ
1037 observations. *Catena* 190, 104535. <https://doi.org/10.1016/j.catena.2020.104535>
- 1038 Fan, F.M., Buarque, D.C., Pontes, P.R.M., Collischonn, W., 2015. Um Mapa de Unidades de
1039 Resposta Hidrológica para a América do Sul. XXI Simpósio Bras. e Recur. Hídricos 1–8.
- 1040 FAO/UNESCO, 1974. FAO/UNESCO Soil Map of the World | Food and Agriculture
1041 Organization of the United Nations [WWW Document]. FAO/UNESCO Soil Map World.
- 1042 Fassoni-Andrade, A.C., Paiva, R.C.D. de, 2019a. Mapping spatial-temporal sediment dynamics
1043 of river-floodplains in the Amazon. *Remote Sens. Environ.* 221, 94–107.
1044 <https://doi.org/10.1016/j.rse.2018.10.038>
- 1045 Fassoni-Andrade, A.C., Paiva, R.C.D. de, 2019b. Mapping spatial-temporal sediment dynamics
1046 of river-floodplains in the Amazon. *Remote Sens. Environ.* 221, 94–107.

- 1047 <https://doi.org/10.1016/j.rse.2018.10.038>
- 1048 Filizola, N., Guyot, J.-L., Wittmann, H., Martinez, J.-M., de, E., 2011. The Significance of
1049 Suspended Sediment Transport Determination on the Amazonian Hydrological Scenario.
1050 Sediment Transp. Aquat. Environ. <https://doi.org/10.5772/19948>
- 1051 Filizola, N., Guyot, J.L., 2011. Fluxo de sedimentos em suspensão nos rios da Amazônia. Rev.
1052 Bras. Geociências 41, 566–576.
- 1053 Filizola, N., Guyot, J.L., 2009. Suspended sediment yields in the Amazon basin: an assessment
1054 using the Brazilian national data set. Hydrol. Process. 23, 3207–3215.
1055 <https://doi.org/10.1002/hyp.7394> Suspended
- 1056 Fleischmann, A., Collischonn, W., Paiva, R., Tucci, C.E., 2019a. Modeling the role of reservoirs
1057 versus floodplains on large-scale river hydrodynamics. Nat. Hazards 99, 1075–1104.
1058 <https://doi.org/10.1007/s11069-019-03797-9>
- 1059 Fleischmann, A., Paiva, R., Collischonn, W., 2019b. Can regional to continental river
1060 hydrodynamic models be locally relevant? A cross-scale comparison. J. Hydrol. X 3,
1061 100027. <https://doi.org/10.1016/j.hydroa.2019.100027>
- 1062 Fleischmann, A., Siqueira, V., Paris, A., Collischonn, W., Paiva, R., Pontes, P., Crétaux, J.F.,
1063 Bergé-Nguyen, M., Biancamaria, S., Gosset, M., Calmant, S., Tanimoun, B., 2018.
1064 Modelling hydrologic and hydrodynamic processes in basins with large semi-arid wetlands.
1065 J. Hydrol. 561, 943–959. <https://doi.org/10.1016/j.jhydrol.2018.04.041>
- 1066 Fluet-Chouinard, E., Lehner, B., Rebelo, L.M., Papa, F., Hamilton, S.K., 2015. Development of
1067 a global inundation map at high spatial resolution from topographic downscaling of coarse-
1068 scale remote sensing data. Remote Sens. Environ. 158, 348–361.
1069 <https://doi.org/dx.doi.org/10.1016/j.rse.2014.10.015>
- 1070 Föeger, L.B., 2019. Modelagem Hidrossedimentológica de Grandes Bacias com Propagação
1071 Inercial de Vazão: estudo de caso da baía do rio Madeira. Federal University of Espírito
1072 Santo.
- 1073 Forsberg, B.R., Melack, J.M., Dunne, T., Barthem, R.B., Goulding, M., Paiva, R.C.D., Sorribas,
1074 M. V., Silva, U.L., Weisser, S., 2017. The potential impact of new Andean dams on
1075 Amazon fluvial ecosystems, PLoS ONE. <https://doi.org/10.1371/journal.pone.0182254>
- 1076 Galy, V., Peucker-Ehrenbrink, B., Eglinton, T., 2015. Global carbon export from the terrestrial
1077 biosphere controlled by erosion. Nature 521, 204–207. <https://doi.org/10.1038/nature14400>
- 1078 García-Ruiz, J.M., Beguería, S., Nadal-Romero, E., González-Hidalgo, J.C., Lana-Renault, N.,
1079 Sanjuán, Y., 2015. A meta-analysis of soil erosion rates across the world. Geomorphology
1080 239, 160–173. <https://doi.org/10.1016/j.geomorph.2015.03.008>
- 1081 Getirana, A.C. V, Paiva, R.C.D., 2013. Mapping large-scale river flow hydraulics in the Amazon
1082 Basin. Water Resour. Res. 49, 2437–2445. <https://doi.org/10.1002/wrcr.20212>
- 1083 Grill, G., Lehner, B., Thieme, M., Geenen, B., Tickner, D., Antonelli, F., Babu, S., Borrelli, P.,
1084 Cheng, L., Crochetiere, H., Ehalt Macedo, H., Filgueiras, R., Goichot, M., Higgins, J.,
1085 Hogan, Z., Lip, B., McClain, M.E., Meng, J., Mulligan, M., Nilsson, C., Olden, J.D.,
1086 Opperman, J.J., Petry, P., Reidy Liermann, C., Sáenz, L., Salinas-Rodríguez, S., Schelle, P.,
1087 Schmitt, R.J.P., Snider, J., Tan, F., Tockner, K., Valdujo, P.H., van Soesbergen, A., Zarfl,
1088 C., 2019. Mapping the world’s free-flowing rivers. Nature 569, 215–221.
1089 <https://doi.org/10.1038/s41586-019-1111-9>
- 1090 Guyot, J., Bourges, J., Calle, H., Cortes, J., Hoorelbecke, R., Roche, M., 1989. Transport of
1091 suspended sediments to the Amazon by the Andean river: The River Mamore, Bolivia, in:
1092 Fourth International Symposium on River Sedimentation. ISRS, Beijing, China. pp. 106–

- 1093 113.
- 1094 Guyot, J.L., Filizola, N., Quintanilla, J., Cortez, J., 1996. Dissolved solids and suspended
1095 sediment yields in the Rio Madeira basin, from the Bolivian Andes to the Amazon. IAHS-
1096 AISH Publ. 236, 55–63.
- 1097 Guyot, J.L., Jouanneau, J.M., Wasson, J.G., 1999. Characterisation of river bed and suspended
1098 sediments in the Rio Madeira drainage basin (Bolivian Amazonia). *J. South Am. Earth Sci.*
1099 12, 401–410. [https://doi.org/10.1016/S0895-9811\(99\)00030-9](https://doi.org/10.1016/S0895-9811(99)00030-9)
- 1100 Hanasaki, N., Kanae, S., Oki, T., 2006. A reservoir operation scheme for global river routing
1101 models. *J. Hydrol.* 327, 22–41.
- 1102 Hanasaki, N., Kanae, S., Oki, T., Masuda, K., Motoya, K., Shirakawa, N., Shen, Y., Tanaka, K.,
1103 2008. An integrated model for the assessment of global water resources – Part 1: Model
1104 description and input meteorological forcing. *Hydrol. Earth Syst. Sci.* 12, 1007–1025.
- 1105 Hanasaki, N., Kanae, S., Oki, T., Masuda, K., Motoya, K., Shirakawa, N., Shen, Y., Tanaka, K.,
1106 2008. An integrated model for the assessment of global water resources – Part 2:
1107 Applications and assessments. *Hydrol. Earth Syst. Sci.* 12, 1027–1037.
- 1108 Hanasaki, N., Yoshikawa, S., Pokhrel, Y., Kanae, S., 2018. A global hydrological simulation to
1109 specify the sources of water used by humans. *Hydrol. Earth Syst. Sci.* 22, 789–817.
- 1110 IDEAM, 2007. Protocolo para el monitoreo y seguimiento del agua.
- 1111 International Standard - ISO, n.d. Measurement of liquid flow in open channels - Methods for
1112 measurement of characteristics of suspended sediment.
- 1113 Ito, A., 2007. Simulated impacts of climate and land-cover change on soil erosion and
1114 implication for the carbon cycle, 1901 to 2100. *Geophys. Res. Lett.*
1115 <https://doi.org/10.1029/2007GL029342>
- 1116 Kettner, A.J., Restrepo, J.D., Syvitski, J.P.M., 2010. A spatial simulation experiment to replicate
1117 fluvial sediment fluxes within the Magdalena River Basin, Colombia. *J. Geol.* 118, 363–
1118 379. <https://doi.org/10.1086/652659>
- 1119 Knisel, W.G., 1980. CREAMS: A Field-Scale Model for Chemicals, Runoff and Erosion for
1120 Agricultural Management Systems.
- 1121 Kollat, J.B., Reed, P.M., Wagener, T., 2012. When are multiobjective calibration trade-offs in
1122 hydrologic models meaningful? *Water Resour. Res.* 48, 1–19.
1123 <https://doi.org/10.1029/2011WR011534>
- 1124 Kouwen, N., Soulis, E.D., Pietroniro, A., Donald, J., HARRINGTON; R. A, 1993. Grouped
1125 Response Units for Distributed Hydrologic Modeling. *J. Water Resour. Plan. Manag.* 119,
1126 289–305.
- 1127 Krysanova, V., Mu, D., Becker, A., 1998. Development and test of a spatially distributed
1128 hydrological/ water quality model for mesoscale watersheds. *Ecol. Model* 106, 261–289.
- 1129 Kuhn, N.J., Hoffmann, T., Schwanghat, W., Dotterwiech, M., 2009. Agricultural soil erosion and
1130 global carbon cycle: controversy over? *Earth Surf. Process. Landforms* 34, 1033–1038.
1131 <https://doi.org/10.1002/esp>
- 1132 Lal, R., 2003. Soil erosion and the global carbon budget. *Environ. Int.* 29, 437–450.
1133 [https://doi.org/10.1016/S0160-4120\(02\)00192-7](https://doi.org/10.1016/S0160-4120(02)00192-7)
- 1134 Latrubesse, E.M., Arima, E.Y., Dunne, T., Park, E., Baker, V.R., D’Horta, F.M., Wight, C.,
1135 Wittmann, F., Zuanon, J., Baker, P.A., Ribas, C.C., Norgaard, R.B., Filizola, N., Ansar, A.,
1136 Flyvbjerg, B., Stevaux, J.C., 2017. Damming the rivers of the Amazon basin. *Nature* 546,
1137 363–369. <https://doi.org/10.1038/nature22333>
- 1138 Latrubesse, E.M., Stevaux, J.C., Sinha, R., 2005. Tropical rivers. *Geomorphology* 70, 187–206.

- 1139 <https://doi.org/10.1016/j.geomorph.2005.02.005>
- 1140 Lehner, B., Liermann, C.R., Revenga, C., Vörösmarty, C., Fekete, B., Crouzet, P., Döll, P.,
1141 Endejan, M., Frenken, K., Magome, J., Nilsson, C., Robertson, J.C., Rödel, R., Sindorf, N.,
1142 Wisser, D., 2011. High-resolution mapping of the world's reservoirs and dams for
1143 sustainable river-flow management. *Front. Ecol. Environ.* 9, 494–502.
1144 <https://doi.org/10.1890/100125>
- 1145 Lehner, B., Verdin, K., Jarvis, A., 2008. New global hydrography derived from spaceborne
1146 elevation data. *Eos (Washington, DC)*. 89, 93–94.
1147 <https://doi.org/https://doi.org/10.1029/2008EO100001>
- 1148 Lima, J.E.F.W., Lopes, W.T. a., De Oliveira Carvalho, N., Vieira, M.R., Da Silva, E.M., 2005.
1149 Suspended sediment fluxes in the large river basins of Brazil. *IAHS ICCE Symp. Sediments*
1150 *Budgets 1* 1, 355–364.
- 1151 Littleboy, M., Silburn, M.D., Freebairn, D.M., Woodruff, D.R., Hammer, G.L., Leslie, J.K.,
1152 1992. Impact of soil erosion on production in cropping systems. I. Development and
1153 validation of a simulation model. *Aust. J. Soil Res.* 30, 757–774.
- 1154 Martín-Vide, J.P., Amarilla, M., Zárata, F.J., 2014. Collapse of the Pilcomayo River.
1155 *Geomorphology* 205, 155–163. <https://doi.org/10.1016/j.geomorph.2012.12.007>
- 1156 Meade, R.H., Weibezahn, F.H., Lewis Jr, W.M., Hernandez, D.P., 1990. Suspended-sediment
1157 budget for the Orinoco River., in: *The Orinoco River as an Ecosystem*. pp. 55–79.
- 1158 Morehead, M.D., Syvitski, J.P., Hutton, E.W.H., Peckham, S.D., 2003. Modeling the temporal
1159 variability in the flux of sediment from ungauged river basins. *Glob. Planet. Change* 39, 95–
1160 110. [https://doi.org/10.1016/S0921-8181\(03\)00019-5](https://doi.org/10.1016/S0921-8181(03)00019-5)
- 1161 Morris, G., Fan, J., 1998. *Reservoir Sedimentation Handbook*. McGraw-Hill Book Co., New
1162 York.
- 1163 Mouyen, M., Longuevergne, L., Steer, P., Crave, A., Lemoine, J.M., Save, H., Robin, C., 2018.
1164 Assessing modern river sediment discharge to the ocean using satellite gravimetry. *Nat.*
1165 *Commun.* 9, 1–9. <https://doi.org/10.1038/s41467-018-05921-y>
- 1166 Müller-Nedebock, D., Chaplot, V., 2015. Soil carbon losses by sheet erosion: A potentially
1167 critical contribution to the global carbon cycle. *Earth Surf. Process. Landforms* 40, 1803–
1168 1813. <https://doi.org/10.1002/esp.3758>
- 1169 Murphy, J., 2019. Declining suspended sediment in United States rivers and streams: Linking
1170 sediment trends to changes in land use/cover, hydrology and climate. *Hydrol. Earth Syst.*
1171 *Sci. Discuss.* 1–37. <https://doi.org/10.5194/hess-2019-435>
- 1172 Naipal, V., Ciais, P., Wang, Y., Lauerwald, R., Guenet, B., Van Oost, K., 2018. Global soil
1173 organic carbon removal by water erosion under climate change and land use change during
1174 AD-1850-2005. *Biogeosciences* 15, 4459–4480. <https://doi.org/10.5194/bg-15-4459-2018>
- 1175 Naipal, V., Reick, C., Pongratz, J., Van Oost, K., 2015. Improving the global applicability of the
1176 RUSLE model - Adjustment of the topographical and rainfall erosivity factors. *Geosci.*
1177 *Model Dev.* 8, 2893–2913. <https://doi.org/10.5194/gmd-8-2893-2015>
- 1178 Nash, J.E., Sutcliffe, J. V, 1970. River Flow Forecasting Through Conceptual Models Part I-a
1179 Discussion of Principles. *J. Hydrol.* 10, 282–290. [https://doi.org/10.1016/0022-](https://doi.org/10.1016/0022-1694(70)90255-6)
1180 [1694\(70\)90255-6](https://doi.org/10.1016/0022-1694(70)90255-6)
- 1181 New, M., Lister, D., Hulme, M., Makin, I., 2002. A high-resolution data set of surface climate
1182 over global land areas. *Clim. Res.* 21, 1–25.
- 1183 Niu, B., Hong, S., Yuan, J., Peng, S., Wang, Z., Zhang, X., 2014. Global trends in sediment-
1184 related research in earth science during 1992-2011: A bibliometric analysis. *Scientometrics*

- 1185 98, 511–529. <https://doi.org/10.1007/s11192-013-1065-x>
- 1186 O’Loughlin, F.E., Paiva, R.C.D., Durand, M., Alsdorf, D.E., Bates, P.D., 2016. A multi-sensor
1187 approach towards a global vegetation corrected SRTM DEM product. *Remote Sens.*
1188 *Environ.* 182, 49–59.
- 1189 Oliveira, P.T.S., Nearing, M.A., Wendland, E., 2015. Orders of magnitude increase in soil
1190 erosion associated with land use change from native to cultivated vegetation in a Brazilian
1191 savannah environment. *Earth Surf. Process. Landforms* 40, 1524–1532.
1192 <https://doi.org/10.1002/esp.3738>
- 1193 Paiva, R.C.D., Buarque, D.C., Collischonn, W., Bonnet, M.P., Frappart, F., Calmant, S.,
1194 Bulhões Mendes, C.A., 2013. Large-scale hydrologic and hydrodynamic modeling of the
1195 Amazon River basin. *Water Resour. Res.* 49, 1226–1243.
1196 <https://doi.org/10.1002/wrcr.20067>
- 1197 Paiva, R.C.D., Collischonn, W., Tucci, C.E.M., 2011. Large scale hydrologic and hydrodynamic
1198 modeling using limited data and a GIS based approach. *J. Hydrol.* 406, 170–181.
1199 <https://doi.org/10.1016/j.jhydrol.2011.06.007>
- 1200 Panagos, P., Borrelli, P., Meusburger, K., Yu, B., Klik, A., Lim, K.J., Yang, J.E., Ni, J., Miao,
1201 C., Chattopadhyay, N., Sadeghi, S.H., Hazbavi, Z., Zabihi, M., Larionov, G.A., Krasnov,
1202 S.F., Gorobets, A. V., Levi, Y., Erpul, G., Birkel, C., Hoyos, N., Naipal, V., Oliveira,
1203 P.T.S., Bonilla, C.A., Meddi, M., Nel, W., Al Dashti, H., Boni, M., Diodato, N., Van Oost,
1204 K., Nearing, M., Ballabio, C., 2017. Global rainfall erosivity assessment based on high-
1205 temporal resolution rainfall records. *Sci. Rep.* 7, 1–12. [https://doi.org/10.1038/s41598-017-](https://doi.org/10.1038/s41598-017-04282-8)
1206 [04282-8](https://doi.org/10.1038/s41598-017-04282-8)
- 1207 Panagos, P., Borrelli, P., Poesen, J., Ballabio, C., Lugato, E., Meusburger, K., Montanarella, L.,
1208 Alewell, C., 2015. The new assessment of soil loss by water erosion in Europe. *Environ.*
1209 *Sci. Policy* 54, 438–447. <https://doi.org/10.1016/j.envsci.2015.08.012>
- 1210 Pelletier, J.D., 2012. A spatially distributed model for the long-term suspended sediment
1211 discharge and delivery ratio of drainage basins. *J. Geophys. Res. Earth Surf.* 117, 1–15.
1212 <https://doi.org/10.1029/2011JF002129>
- 1213 Phinzi, K., Ngetar, N.S., 2019. The assessment of water-borne erosion at catchment level using
1214 GIS-based RUSLE and remote sensing: A review. *Int. Soil Water Conserv. Res.*
1215 <https://doi.org/10.1016/j.iswcr.2018.12.002>
- 1216 Pontes, P.R.M., 2016. Modelagem hidrológica e hidrodinâmica integrada da bacia do Prata.
1217 Universidade Federal do Rio Grande do Sul.
- 1218 Pontes, P.R.M., Fan, F.M., Fleischmann, A.S., Paiva, R.C.D., Buarque, D.C., Siqueira, V.A.,
1219 Jardim, P.F., Sorribas, M.V., Collischonn, W., 2017. MGB-IPH model for hydrological and
1220 hydraulic simulation of large floodplain river systems coupled with open source GIS.
1221 *Environ. Model. Softw.* 94, 1–20.
- 1222 Restrepo, J.D., Kjerfve, B., Hermelin, M., Restrepo, J.C., 2006. Factors controlling sediment
1223 yield in a major South American drainage basin: The Magdalena River, Colombia. *J.*
1224 *Hydrol.* 316, 213–232. <https://doi.org/10.1016/j.jhydrol.2005.05.002>
- 1225 Rivera, I.A., Cardenas, E.A., Espinoza-Villar, R., Espinoza, J.C., Molina-Carpio, J., Ayala, J.M.,
1226 Gutierrez-Cori, O., Martinez, J.M., Filizola, N., 2019. Decline of fine suspended sediments
1227 in the Madeira River basin (2003-2017). *Water (Switzerland)* 11.
1228 <https://doi.org/10.3390/w11030514>
- 1229 Rudorff, C.M., Dunne, T., Melack, J.M., 2018. Recent increase of river–floodplain suspended
1230 sediment exchange in a reach of the lower Amazon River. *Earth Surf. Process. Landforms*

- 1231 43, 322–332. <https://doi.org/10.1002/esp.4247>
- 1232 Sadeghi, S.H.R., Gholami, L., Khaledi Darvishan, A., Saeidi, P., 2014. A review of the
1233 application of the MUSLE model worldwide. *Hydrol. Sci. J.* 59, 365–375.
1234 <https://doi.org/10.1080/02626667.2013.866239>
- 1235 Santini, W., Camenen, B., Le Coz, J., Vauchel, P., Guyot, J.-L., Lavado, W., Carranza, J.,
1236 Paredes, M.A., Pérez Arévalo, J.J., Arévalo, N., Espinoza Villar, R., Julien, F., Martinez, J.-
1237 M., 2019. An index concentration method for suspended load monitoring in large rivers of
1238 the Amazonian foreland. *Earth Surf. Dyn.* 7, 515–536. <https://doi.org/10.5194/esurf-2018-93>
- 1239
- 1240 Sartori, M., Philippidis, G., Ferrari, E., Borrelli, P., Lugato, E., Montanarella, L., Panagos, P.,
1241 2019. A linkage between the biophysical and the economic: Assessing the global market
1242 impacts of soil erosion. *Land use policy* 86, 299–312.
1243 <https://doi.org/10.1016/j.landusepol.2019.05.014>
- 1244 Schmidt, G.W., 1972. Amounts of suspended solids and dissolved substances in the middle
1245 reaches of the Amazon over the course of one year. *Amazoniana* 3, 208–223.
- 1246 Shen, Z.Y., Chen, L., Chen, T., 2012. Analysis of parameter uncertainty in hydrological
1247 modeling using GLUE method: a case study of SWAT model applied to Three Gorges
1248 Reservoir Region, China. *Hydrol. Earth Syst. Sci. Discuss.* 8, 8203–8229.
1249 <https://doi.org/10.5194/hessd-8-8203-2011>
- 1250 Shin, S., Pokhrel, Y., Miguez-Macho, G., 2019. High-resolution modeling of reservoir release
1251 and storage dynamics at the continental scale. *Water Resources Res.* 55, 787–810.
- 1252 Siqueira, V.A., Paiva, R.C.D., Fleischmann, A.S., Fan, F.M., Anderson, L., Pontes, P.R.M.,
1253 Paris, A., Calmant, S., Collischonn, W., 2018. Toward continental hydrologic –
1254 hydrodynamic modeling in South America. *Hydrol. Earth Syst. Sci.* 22, 4815–4842.
1255 <https://doi.org/doi.org/10.5194/hess-22-4815-2018>
- 1256 Syvitski, J.P.M., Cohen, S., Kettner, A.J., Brakenridge, G.R., 2014. How important and different
1257 are tropical rivers? - An overview. *Geomorphology* 227, 5–17.
1258 <https://doi.org/10.1016/j.geomorph.2014.02.029>
- 1259 Syvitski, J.P.M., Milliman, J.D., 2007. Geology, Geography, and Humans Battle for Dominance
1260 over the Delivery of Fluvial Sediment to the Coastal Ocean. *J. Geol.* 115, 1–19.
1261 <https://doi.org/10.1086/509246>
- 1262 Syvitski, J.P.M., Vörösmarty, C.J., Kettner, A.J., Green, P., 2005. Impact of Humans on the Flux
1263 of Terrestrial Sediment to the Global Coastal Ocean. *Science* (80-.). 308, 376–380.
- 1264 Tan, Z., Leung, L.R., Li, H., Tesfa, T., Vanmaercke, M., Poesen, J., Zhang, X., Lu, H.,
1265 Hartmann, J., 2017. A Global Data Analysis for Representing Sediment and Particulate
1266 Organic Carbon Yield in Earth System Models. *Water Resour. Res.* 53, 10674–10700.
1267 <https://doi.org/10.1002/2017WR020806>
- 1268 Tan, Z., Leung, L.R., Li, H.Y., Tesfa, T., 2018. Modeling Sediment Yield in Land Surface and
1269 Earth System Models: Model Comparison, Development, and Evaluation. *J. Adv. Model.*
1270 *Earth Syst.* 10, 2192–2213. <https://doi.org/10.1029/2017MS001270>
- 1271 van Beek, L.P.H., Wada, Y., Bierkens, M.F.P., 2011. Global monthly water stress: 1. Water
1272 balance and water availability. *Water Resources Res.* 47.
1273 <https://doi.org/doi:10.1029/2010WR009791>
- 1274 Van Oost, K., Quine, T.A., Govers, G., De Gryze, S., Six, J., Harden, J.W., Ritchie, J.C.,
1275 McCarty, G.W., Heckrath, G., Kosmas, C., Giraldez, J. V., Marques Da Silva, J.R., Merckx,
1276 R., 2007. The impact of agricultural soil erosion on the global carbon cycle. *Science* (80-.).

- 1277 318, 626–629. <https://doi.org/10.1126/science.1145724>
- 1278 Villar, J.C.E., Ronchail, J., Guyot, J.L., Cochonneau, G., Filizola, N., Lavado, W., de Oliveira,
1279 E., Pombosa, R., Vauchel, P., 2008. Spatio-temporal rainfall variability in the Amazon
1280 basin countries (Brazil, Peru, Bolivia, Colombia, and Ecuador). *Int. J. Climatol.* 2009,
1281 1574–1594. <https://doi.org/10.1002/joc>
- 1282 Wada, Y., Wisser, D., Bierkens, M.F.P., 2014. Global modeling of withdrawal, allocation and
1283 consumptive use of surface water and groundwater resources. *Earth Syst. Dyn. Discuss.* 5,
1284 15–40.
- 1285 Wang, Z., Van Oost, K., 2019. Modeling global anthropogenic erosion in the Holocene.
1286 *Holocene* 29, 367–379. <https://doi.org/10.1177/0959683618816499>
- 1287 Willenbring, J.K., Von Blanckenburg, F., 2010. Long-term stability of global erosion rates and
1288 weathering during late-Cenozoic cooling. *Nature* 465, 211–214.
1289 <https://doi.org/10.1038/nature09044>
- 1290 Williams, J.R., 1995. The EPIC model, in: *Computer Models of Watershed Hydrology*. pp. 909–
1291 1000.
- 1292 Williams, J.R., 1975. SEDIMENT ROUTING FOR AGRICULTURAL WATERSHEDS '.
1293 *Water Resour. Bull.* 11.
- 1294 Wischmeier, W., Smith, D., 1978. Predicting rainfall erosion losses: a guide to conservation
1295 planning, U.S. Department of Agriculture Handbook No. 537.
1296 <https://doi.org/10.1029/TR039i002p00285>
- 1297 Wisser, D., Fekete, B.M., Vörösmarty, C.J., Schumann, A.H., 2010. Reconstructing 20th century
1298 global hydrography: A contribution to the Global Terrestrial Network- Hydrology (GTN-
1299 H). *Hydrol. Earth Syst. Sci.* 14, 1–24. <https://doi.org/10.5194/hess-14-1-2010>
- 1300 Wood, E.F., Roundy, J.K., Troy, T.J., van Beek, L.P.H., Bierkens, M.F.P., Blyth, E., et al, 2011.
1301 Hyperresolution global land surface modeling: meeting a grand challenge for monitoring
1302 Earth's terrestrial water. *Water Resour. Res.* 47, 1–10.
- 1303 Wu, W., Wang, S.S.Y., 2006. Formulas for sediment porosity and settling velocity. *J. Hydraul.*
1304 *Eng.* 132, 858–862.
- 1305 Wuepper, D., Borrelli, P., Finger, R., 2019. Countries and the global rate of soil erosion. *Nat.*
1306 *Sustain.* 1–5. <https://doi.org/10.1038/s41893-019-0438-4>
- 1307 Xiong, M., Sun, R., Chen, L., 2019. A global comparison of soil erosion associated with land use
1308 and climate type. *Geoderma* 343, 31–39. <https://doi.org/10.1016/j.geoderma.2019.02.013>
- 1309 Xiong, M., Sun, R., Chen, L., 2018. Effects of soil conservation techniques on water erosion
1310 control: A global analysis. *Sci. Total Environ.* 645, 753–760.
1311 <https://doi.org/10.1016/j.scitotenv.2018.07.124>
- 1312 Yamazaki, D., de Almeida, G.A.M., Bates, P.D., 2013. Improving computational efficiency in
1313 global river models by implementing the local inertial flow equation and a vector-based
1314 river network map. *Water Resources Res.* 49, 7221–7235.
- 1315 Yamazaki, D., Kanae, S., Kim, H., Oki, T., 2011. A physically based description of floodplain
1316 inundation dynamics in a global river routing model. *Water Resources Res.* 47.
- 1317 Yang, C.T., 1973. Incipient motion and sediment transport. *J. Hydraul. Eng.* 10, 1679–1704.
- 1318 Yang, D., Kanae, S., Oki, T., Koike, T., Musiak, K., 2003. Global potential soil erosion with
1319 reference to land use and climate changes. *Hydrol. Process.* 17, 2913–2928.
1320 <https://doi.org/10.1002/hyp.1441>
- 1321 Yapo, P.O., Gupta, H.V., Sorooshian, S., 1998. Multi-objective global optimization for
1322 hydrologic models. *J. Hydrol.* 204, 83–97. [https://doi.org/10.1016/S0022-1694\(97\)00107-8](https://doi.org/10.1016/S0022-1694(97)00107-8)

- 1323 Zhang, K., Douglas, B.C., Leatherman, S.P., 2004. Global warming and coastal erosion. *Clim.*
1324 *Change* 64, 41–58. <https://doi.org/10.1023/B:CLIM.0000024690.32682.48>
- 1325 Zhao, F., Veldkamp, T.I.E., Frieler, K., Schewe, J., Ostberg, S., Willner, S., Schauburger, B.,
1326 Gosling, S.N., Schmied, H.M., Portmann, F.T., Leng, G., Huang, M., Liu, X., Tang, Q.,
1327 Hanasaki, N., Biemans, H., Gerten, D., Satoh, Y., Pokhrel, Y., Stacke, T., Ciais, P., Chang,
1328 J., Ducharne, A., Guimberteau, M., Wada, Y., Kim, H., Yamazaki, D., 2017. The critical
1329 role of the routing scheme in simulating peak river discharge in global hydrological models.
1330 *Environ. Res. Lett.* 12. <https://doi.org/10.1088/1748-9326/aa7250>
1331